Slippage effect on interfacial destabilization driven by standing surface acoustic waves under hydrophilic conditions

J. Muñoz [1] J. Arcos [2,*] I. Campos-Silva,[1] O. Bautista [2,†] and F. Méndez [3]

[1]*Instituto Politécnico Nacional, Avenida Luis Enrique Erro, Unidad Profesional Adolfo López Mateos, Zacatenco, Gustavo A. Madero, Ciudad de México 07738, Mexico*
[2]*Instituto Politécnico Nacional, Avenida de las Granjas 682, Colonia Santa Catarina, Azcapotzalco, Ciudad de México 02250, Mexico*
[3]*Universidad Nacional Autónoma de México, Coyoacan, Ciudad de México 04510, Mexico*

In the present work, we theoretically analyze the influence of the slippage phenomenon on the atomization via surface acoustic waves of a millimeter-order water drop deposited over a hydrophilic substrate. The analysis is conducted by considering, in the first place, a standing surface acoustic wave acting at the free surface of the parent drop. Subsequently, the lubrication theory is applied to the flow field governing equations to derive an evolution equation of the air-liquid interface in terms of the acoustic capillary number and the Navier-slip coefficient. Such an equation's numerical solution leads to a simplified drop model, depicting the spatiotemporal deformation of the free surface under the influence of slippage phenomenon and predicts the atomization threshold once the instability length at the induced capillary waves is achieved. Our numerical simulations show that the high-frequency acoustic excitation under consideration leads to the development of a standing wave at the free surface, which oscillates at a viscous-capillary resonance frequency on order 10^4 Hz. Moreover, a spreading phenomenon on the fluid drop is induced, strongly linked to the magnitude of the acoustic capillary number. In this scenario, the slippage under hydrophilic conditions has a noticeable impact on the free surface dynamics, causing smaller aerosol characteristic diameters in comparison with the no-slip case. In this context, the present study provides an analytical expression that calculates the droplet diameter in terms of the slip coefficient. In the process, we postulate the slippage phenomenon as a valuable means to control the parent drop's deformation mechanism and, therefore, the aerosol characteristic diameter.

I. INTRODUCTION

In recent decades, there has been significant progress in the development of microfluidics due to the possibility of integrating several tasks related to mixing, separation, or trapping of microparticle suspensions in only one small-scale device, known as *Lab-on-a-Chip* (LOC) [1,2]. Microfluidics involves the study and development of many microparticle handling techniques [2–6], which assures fluid movement and particle transport, essential aspects for enhancing the reliability and efficiency of the LOC's. Among these techniques, we can find the acoustofluidics, which is defined as the ultrasound-based external forcing of microparticles in microfluidics. It has traditionally been relevant due to the exploitation of two physical phenomena: *acoustic streaming* [7] and *acoustophoresis*,

---

*jarcos@ipn.mx
†obautista@ipn.mx

both of them allowing label-free particle manipulation based only on its mechanical properties, e.g., size, density, or compressibility, which is desirable for mixing, or separation of immersed particulate matter. Typically, the external acoustic forcing in microfluidic systems derives from ultrasonic mechanical vibrations [8,9], generating Reynolds stresses in the fluid and the acoustic radiation force [10], both are fundamental mechanisms in acoustic streaming and acoustophoresis. However, the influence of ultrasonic acoustic waves on a fluid can derive in another mechanism of particular interest for our study, for particle manipulation in microfluidics systems, called *ultrasonic atomization*.

Ultrasound-based atomization technique [10–12] generates micron- and submicron-sized aerosol droplets by applying an ultrasonic acoustic field (up to 3 MHz) over the free surface of liquid solutions. Specifically, the mechanical energy applied from a piezoelectric device agitates the air-liquid interface of the solution, promoting the formation and subsequent breakup of cavitation bubbles, which is the main mechanism behind the formation and ejection of monodispersed droplets at the free surface. Such aerosol generation process provide small droplets with potential applications in analytical chemistry or medicine [13,14]. Over the years, ultrasonic atomization technique increased its popularity in microfluidics, although crucial features, like miniaturization and portability, constituted serious obstacles that hindered its full implementation at small-scale systems. In the 1990s, these disadvantages were attended with the development of a particular type of ultrasonic atomization technique, called *SAW atomization* [15–22]. This technique consists of using a nanometer-order mechanical disturbance termed *surface acoustic waves* (SAW) [23,24], which operates at frequencies from 10 to 500 MHz, several orders of magnitude above conventional ultrasonic atomization. SAW atomization process relies on the formation, and subsequent breakup of capillary waves via capillary instability [25] at the air-liquid interface of small-scale fluid drops placed over piezoelectric substrates, therefore, micron- and submicron-sized aerosol droplets are generated from the parent drop. SAW atomization is an excellent medium for mass and heat transfer in LOC's, therefore is commonly implemented in microfluidic systems destined for pulmonary drug delivery [15,19,21,22], mass spectrometry [26], cooling [16] or even as a promising technology for *paper-based microfluidics* [27], by allowing, for example, to successfully extract protein molecules from hydrophilic cellulose papers [20].

A clear and deep understanding of the physics behind the formation and evolution of capillary waves at the air-liquid interface of a drop exposed to acoustic forcing is necessary to provide a reliable and efficient usage of SAW atomization. In this context, the deformation mechanisms occurring at the free surface of a drop are directly related to the atomization rate and the characteristic diameter of aerosol. However, the presence of multiple lengths and time scales in the phenomenon, high droplet ejection velocities or even *capillary wave turbulence* [28], represent formidable challenges that prevent experimental studies from properly portray the dynamics of the air-liquid interface under SAW excitation and its dependence of fluid properties. Nevertheless, numerical simulations have proven to give a valuable insight regarding the formation of capillary waves and their destabilization mechanism before atomization process [18,29–31]. For example, Qi *et al.* [18] studied the destabilization phenomenon in terms of the *acoustic capillary number*. In this context, by developing a numerical model based on the lubrication theory, their study managed to capture the resulting deformations at the drop's free surface. When the curvature gradients portrayed by the model were sufficiently strong, a reasonable prediction of the *instability threshold*—indicating imminent drop atomization—was given. Moreover, endorsed by experimental evidence, Qi's study predicted the characteristic diameter of the ejected droplets, $d \sim \lambda_{inst}$, where λ_{inst} is the instability wavelength. The subsequent study developed by Tan *et al.* [31] illustrated how computational analysis could be applied to incorporate the coupling between the piezoelectric substrate and the liquid drop into the interfacial deformation analysis. Their research effort delivered useful and reliable data regarding capillary wave motion and even predict the development of interesting phenomena not yet experimentally reported, like the *superharmonic frequencies*, which appear at the drop's free surface under low-amplitude regimes of SAW excitation.

Considering the literature cited above, the deformation mechanism at the air-liquid interface induced by SAWs constitutes a complex mechanism. Capillary and viscous stresses at the drop's interface determine the formation of liquid threads its subsequent breakup into aerosol droplets. In this context, our study constitutes a computational effort developed to broaden the comprehension of the destabilization process leading SAW atomization by considering a topic that has proven to be of fundamental physical interest. It can exert significant repercussions in many areas of engineering and applied sciences where liquids interact with microfluidic devices: *the slippage phenomenon at a solid boundary* [32]. The presence of slippage in any phenomenon is portrayed by imposing a boundary condition on the solid-fluid interface known as the *Navier slip condition*, which for a Newtonian fluid is given by

$$\mathbf{u} - (\mathbf{u} \cdot \mathbf{n})\mathbf{n} - \beta\{\mathbf{E} \cdot \mathbf{n} - [(\mathbf{E} \cdot \mathbf{n}) \cdot \mathbf{n}]\mathbf{n}\} = \mathbf{0}. \tag{1}$$

Here, $\mathbf{n}$ is the unit vector normal to the surface directed into the fluid, $\mathbf{u}$ is the velocity of the fluid, $\mathbf{E}$ is the rate-of-strain tensor, and β is an empirical parameter known as the *slip length*, which possesses units of length and is expected to be of molecular dimensions. Slippage studies like the one provided by Watanabe *et al.* [33] illustrates how the concept of *contact angle* can be used for predicting the presence of slippage phenomenon on solid surfaces. Moreover, a considerable amount of subsequent experimental evidence [34] has shown the slip coefficient (β) has a more relative significance at micron- and submicron scales. In this context we note that the slip coefficient has been quantified as $10^{-9} \leqslant \beta(\text{m}) \leqslant 10^{-6}$ for systems with complete [35–38] and partial [39–46] wetting (i.e., $\theta_c < 90°$). Such systems consisted of fluids like water, sucrose, or hexadecane in contact with surfaces based on silicon, glass, mica, and silica; i.e., a set of fluid and solid materials which are not beyond the scope of microfluidic devices and drop handling techniques.

The present study aims to theoretically evaluate the influence of the Navier slip condition on the interfacial destabilization mechanism of a liquid drop subjected to SAW atomization. In this context, let us note that the usage of slippage phenomenon under hydrophobic conditions (i.e., with $\theta_c > 90°$) for drop handling techniques via SAWs is not an unknown topic. For example, by applying a Teflon-based layer on the piezoelectric substrate, spreading the drop under acoustic excitation is prevented, which constitutes a useful mean for keeping the drop fixed in a particular area and promote the development of phenomena like *interfacial jetting* [47,48]. However, until our knowledge, the direct relationship of the Navier slip coefficient with the deformation mechanism leading toward destabilization and the interfacial breakup of a drop subject to SAW atomization has not yet explored under hydrophilic conditions (i.e., $\theta_c < 90°$). Moreover, being aware of the important role that the *geometric aspect ratio* of the drop plays on the aerosol generation process, as a key parameter which influences the capillary-acoustic stress balance at the air-liquid interface [18], and therefore the diameter of the ejected droplets [49], we explore the influence of slippage under hydrophilic conditions to modify and control the aspect ratio and therefore SAW atomization. Our study implements the lubrication theory to derive an evolution equation governing the drop's free surface response to SAW excitation. By solving such an equation, we analyze the capillary deformations leading toward interfacial breakup and atomization. In this sense, our approach is similar to the numerical work developed by Qi *et al.* [18]; however, our study evaluates the fundamentals of SAW atomization in a completely different scenario, one which assumes slippage in systems with partial and complete wetting (i.e., $\theta_c < 90°$). Although experimentally confirmed and reported, little effort has been dedicated to proving its impact at small-scale phenomena like SAW atomization, a technique where the proper understanding of capillary instability and its connection with fluid properties, like the wettability, is of fundamental importance.

II. PROBLEM FORMULATION

A Newtonian slender drop modeled as a thin liquid film on a two-dimensional framework is deposited over a hydrophilic substrate and exposed to the influence of a high-frequency acoustic field, as depicted in Fig. 1. We assume, based on specialized literature regarding SAW atomization
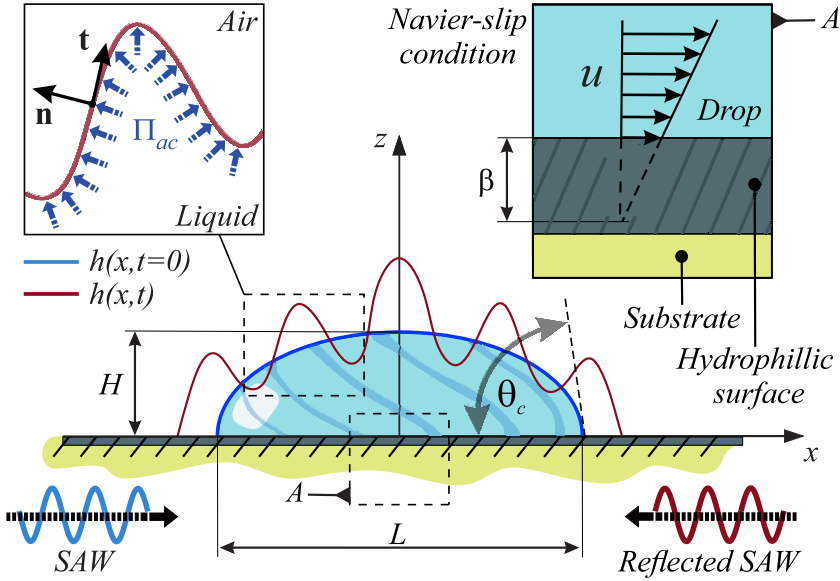
FIG. 1. Evolution of the free surface $h(x, t)$, of a slender drop (with $H \ll L$) due to the excitation forcing $\Pi_{ac}(x, t)$ by a standing SAW that propagates from the substrate to the interface, acting in the direction of the unit normal vector (**n**). An initial drop profile, $h(x, 0) = H \exp[-20(x/L)^2]$ [18], with a contact angle θ_c below $90°$ is considered. The slender drop is subject to the Navier slip condition at the solid-liquid boundary once acoustic excitation begins (See inset *A*). This scenario traduces in implementing a hydrophilic material, placed between the substrate and the drop, which allows a nonzero tangential fluid velocity u at the wall.

[18,49], that the thin film has a length $L(\mathrm{m}) \sim 10^{-3} - 10^{-4}$ and a thickness $H(\mathrm{m}) \sim 10^{-4} - 10^{-5}$, thus, an aspect ratio $H/L \ll 1$ is feasible. Besides, the effect of a certain degree of slip at the solid-liquid interface, quantified by the slip length β, is also considered. Under these circumstances, our study aims to use the lubrication theory to determine the spatiotemporal evolution of the drop's free surface denoted by $h(x, t)$ under SAW excitation. Cartesian coordinates are chosen, such that the x axis is directed along the solid surface, and the z axis is normal to it. When a thin film is exposed to the influence of acoustic stress, velocity and pressure distributions are developed inside the liquid, in concordance with our simplified approach, and we assume such distributions do not change in the direction of y (normal to the plane of the sketch).

To determine the resulting film thickness $h(x, t)$, we consider the influence of an acoustic stress, denoted by Π_{ac}. Such stress, also called *acoustic pressure*, acts in a direction normal to our small-scale drop model's free surface and is responsible for its deformation. We neglect the influence of tangential stresses induced by air and any effect induced by surface tension gradients (like thermocapillary flow); in this sense, we assume constant properties at the liquid film. Worth noting at this point is the absence of any disjoining pressure effect at our lubrication-type drop model. The above is because we do not implement a precursor film model to portray the three-phase contact line; instead, we use an equivalent model, i.e., the Navier-slip boundary condition. Kalliadasis have discussed the equivalence between such models and Chang [50] and Yeo and Chang [51]. Thus, because of the considerations just referred to, the Navier-Stokes and continuity equations for the two-dimensional flow in the liquid film of density ρ and viscosity μ are:

$$\partial_x u + \partial_z w = 0, \tag{2a}$$

$$\rho(\partial_t u + u\partial_x u + w\partial_z u) = -\partial_x p + \mu\nabla^2 u, \tag{2b}$$

$$\rho(\partial_t w + u\partial_x w + w\partial_z w) = -\partial_z p + \mu\nabla^2 w. \tag{2c}$$

Here, u and w are the velocity components in x and z directions, respectively. ∇^2 stands for the Laplacian operator defined by $\nabla = (\partial^2/\partial x^2, \partial^2/\partial z^2)$. The boundary conditions between the liquid and the solid substrate are those of impermeability, given by

$$w = 0 \quad \text{at} \quad z = 0, \tag{3}$$

and the Navier slip condition, which allows tangential relative motion at $z = 0$:

$$u - \beta \partial_z u = 0 \quad \text{at} \quad z = 0, \tag{4}$$

where β is the *slip coefficient*. At the interface, i.e., at $z = h(x, t)$, two main boundary conditions are established; the first one is the so-called kinematic boundary condition, which is given by

$$w = \partial_t h + u\, \partial_x h \quad \text{at} \quad z = h(x, t). \tag{5}$$

Equation (5) represents the balance between the normal component of the liquid velocity at the interface and the speed of the interface. The second boundary condition is obtained by considering a force balance at the air-liquid interface, i.e.,

$$(\mathbf{T} - \hat{\mathbf{T}}) \cdot \mathbf{n} - \sigma \mathbf{n}(\nabla \cdot \mathbf{n}) = \mathbf{f} \quad \text{at} \quad z = h(x, t), \tag{6}$$

where the total stress tensor exerted above the interface by the air and the stress applied by the liquid from beneath the interface is $(\mathbf{T}, \hat{\mathbf{T}})$, respectively. The normal and tangential (unit) vectors are $\mathbf{n}$ and $\mathbf{t}$ (see Fig. 1), and σ is the surface tension. The vector quantity $\mathbf{f}$ represents any prescribed force at the drop's interface, and for our analysis, it contains only one component normal to the interface, the *acoustic force*, denoted by $\mathbf{\Pi}_{\text{ac}}$.

The stresses balance given in Eq. (6) is defined as $\mathbf{T} = -p_{\text{atm}}\mathbf{I} + \boldsymbol{\tau}$ and $\hat{\mathbf{T}} = -\hat{p}\mathbf{I} + \hat{\boldsymbol{\tau}}$, where p_{atm} and $\hat{p}$ represent the total pressure on the two sides of the interface (air-liquid), including both dynamic and hydrostatic contributions. Moreover, $\mathbf{I}$ is the identity matrix, with $\boldsymbol{\tau}$ and $\hat{\boldsymbol{\tau}}$ denoting the viscous stress tensors, respectively. As the viscosity of air is smaller than the liquid one, $\boldsymbol{\tau} = \mathbf{0}$. Taking the inner product of Eq. (6) with the unit vector $\mathbf{n}$, the normal-stress balance at the interface can be rewritten as

$$\hat{p} - p_{\text{atm}} - (\hat{\boldsymbol{\tau}} \cdot \mathbf{n}) \cdot \mathbf{n} + \Pi_{\text{ac}} = \sigma(\nabla \cdot \mathbf{n}) \quad \text{at} \quad z = h(x, t). \tag{7}$$

Note that $\Pi_{ac} = \mathbf{f} \cdot \mathbf{n}$ represents the acoustic pressure. Equation (7) establishes that the normal component of the total stress on the interface undergoes a jump, which is quantified the surface tension times the curvature $\nabla \cdot \mathbf{n}$.

Next, we proceed to detail the features behind the acoustic pressure forcing, Π_{ac}, employed during our study. Let us note in the first place that SAW atomization makes use of Rayleigh waves which possess a *retrograde motion*. The above means that for an acoustic wave traveling from left to right, any particle on the solid surface of the substrate (plane xy in Fig. 1) describes an ellipsoidal trajectory in a counterclockwise fashion, on a plane normal to the surface and parallel to the direction of wave propagation (x axis). Under these circumstances, we model the vibration velocity $\mathfrak{U}$, at the solid surface, by the following expression [52]:

$$\mathfrak{U} = A\, \Omega \cos\theta_R\, e^{i\kappa x} e^{i\Omega t}, \tag{8}$$

Equation (8) indicates that the surface of the piezoelectric substrate is forced to oscillate as a *traveling wave* with an amplitude $A(\text{m}) \sim 10^{-9}$, an angular frequency $\Omega(\text{rad/s}) \sim 10^8$, and with a wave number $\kappa(\text{m}^{-1}) \sim 10^4$. The quantity $\cos\theta_R$ takes into account the diffraction phenomenon of the SAW into the water drop. Such phenomenon, quantified by the *Rayleigh angle* θ_R [24], occurs due to the difference at the sound wave propagation speed between the two media, i.e., the substrate material (commonly a piezoelectric material such as lithium niobate) and the water drop placed over it. The vibration velocity allows estimating the acoustic pressure in the following form [53]:

$$\tilde{\Pi}_{\text{ac}} = \rho\, \mathfrak{U}^2 = \rho A^2 \Omega^2 \cos^2\theta_R\, e^{2i\kappa x} e^{2i\Omega t}. \tag{9}$$

Equation (9) represents an *acoustic traveling wave* [52], which in conjunction with *acoustic standing waves* [54], constitutes typical excitation forcing, implemented on SAW atomization. These waves propagate along the substrate and cause interfacial destabilization at the time they diffract into the drop. We note that the sound wave propagation across the substrate beneath the drop depends on the boundary conditions imposed along the wave propagation path. In this context, a standing wave is generated by allowing the acoustic excitation Eq. (9) to reflect off the free edge of the substrate and interfere with itself (see Fig. 1). If the acoustic excitation Eq. (9) is absorbed by utilizing gel-based substances (e.g., polydimethylsiloxane or α-gel) on the surface of the substrate, then an acoustic excitation via a traveling wave will arise. Specifically, our study considers the influence of a standing wave on a drop placed above a substrate with slippage at the wall. Thus, it is necessary to consider the reflection and subsequent superposition of Eq. (9). Specifically, the acoustic pressure, Π_{ac} used on our study is the sum of a harmonic wave traveling to the right along the x axis, and an identical harmonic wave that is traveling to the left. Because of the above, the acoustic forcing implemented during the present study to calculate the thickness, $h(x,t)$, of our slender drop model is

$$\Pi_{\mathrm{ac}} = 2\rho A^2 \Omega^2 \cos^2 \theta_R \sin(2\kappa x) \cos(2\Omega t). \tag{10}$$

Now we proceed to derive the tangential component of the stress balance at the air-liquid interface. To do that, we take the inner product of Eq. (6) with the tangential (unit) vector to the interface **t** (see also Fig. 1), yielding

$$(\hat{\boldsymbol{\tau}} \cdot \mathbf{n}) \cdot \mathbf{t} = 0 \quad \text{at} \quad z = h(x,t). \tag{11}$$

The vectorial quantities **n** and **t** are defined in terms of the interface shape, $h(x,t)$, as follows:

$$\mathbf{n} = \frac{(-\partial_x h, 1)}{[1 + (\partial_x h)^2]^{1/2}} \quad \text{and} \quad \mathbf{t} = \frac{(1, \partial_x h)}{[1 + (\partial_x h)^2]^{1/2}}. \tag{12}$$

The problem to be solved is formulated in terms of the dimensionless variables defined as

$$\bar{x} \equiv \frac{x}{L}, \quad (\bar{z}, \bar{h}) \equiv \frac{z, h}{H}, \quad \bar{u} \equiv \frac{u}{U}, \quad \bar{w} \equiv \frac{w}{\varepsilon U}, \quad \bar{t} \equiv \frac{t}{L/U}, \quad \bar{p} \equiv \frac{\hat{p} - p_{\mathrm{atm}}}{\varepsilon \sigma / L}. \tag{13}$$

Here, the characteristic pressure $\varepsilon \sigma / L$ in Eqs. (13) was determined by balancing the pressure difference at the interface, $\hat{p}$–p_{atm} with the *capillary pressure*, $\sigma(\nabla \cdot \mathbf{n})$, from the normal stress balance condition given by Eq. (7). Furthermore, the dimensionless parameter $\varepsilon \equiv H/L$ and it is assumed very small compared with unity. The characteristic velocity U is obtained from a viscous-capillary force balance at the interface $\sigma H/L^2 \sim \mu U/H$, then, solving for U yields $U \sim \sigma \varepsilon^2 / \mu$. Using the dimensionless variables defined in Eqs. (13) into the set of Eqs. (2a)–(2c) yields the following dimensionless governing equations:

$$\partial_{\bar{x}} \bar{u} + \partial_{\bar{z}} \bar{w} = 0, \tag{14}$$

$$\mathrm{Re}\, \varepsilon[\partial_{\bar{t}} \bar{u} + \bar{u} \partial_{\bar{x}} \bar{u} + \bar{w} \partial_{\bar{z}} \bar{u}] = -Ca^{-1} \varepsilon^3 \, \partial_{\bar{x}} \bar{p} + \varepsilon^2 \partial_{\bar{x}}^2 u + \partial_{\bar{z}}^2 u, \tag{15a}$$

$$\mathrm{Re}\, \varepsilon^3[\partial_{\bar{t}} \bar{w} + \bar{u} \partial_{\bar{x}} \bar{w} + \bar{w} \partial_{\bar{z}} \bar{w}] = -\partial_{\bar{z}} \bar{p} + \varepsilon^2 (\varepsilon^2 \partial_{\bar{x}}^2 w + \partial_{\bar{z}}^2 w), \tag{15b}$$

where $\mathrm{Re} = UH/\nu$ is the Reynolds number, and $Ca = \mu U/\sigma$ is the capillary number, which measures the importance of viscous effects relative to surface tension. Moreover, the boundary conditions between the liquid and the solid substrate (at $\bar{z} = 0$) in the dimensionless form are

$$\bar{w} = 0 \quad \text{and} \quad \bar{u} - \beta_0 \partial_{\bar{z}} \bar{u} = 0. \tag{16}$$

Here, $\beta_0 = \beta/H$ is the dimensionless slip coefficient. Considering the unit vectors **n** and **t** in Eq. (12) for the stress balance components, the boundary conditions in Eqs. (5), (7), and (11) at

$\bar{z} = \bar{h}(\bar{x}, \bar{t})$ are expressed as

$$\partial_{\bar{t}}\bar{h} + \bar{u}\,\partial_{\bar{x}}\bar{h} = \bar{w}, \tag{17}$$

$$\bar{p} + \bar{\Pi}_{\text{ac}} + \frac{2\varepsilon^2\{\partial_{\bar{x}}\bar{u}[1 - \varepsilon^2(\partial_{\bar{x}}\bar{h})^2] + \partial_{\bar{x}}\bar{h}[\varepsilon^2\partial_{\bar{x}}\bar{w} + \partial_{\bar{z}}\bar{u}]\}}{1 + \varepsilon^2(\partial_{\bar{x}}\bar{h})^2} = \frac{-\partial_{\bar{x}}^2\bar{h}}{[1 + \varepsilon^2(\partial_x\bar{h})^2]^{3/2}}, \tag{18}$$

and

$$[1 - \varepsilon^2(\partial_{\bar{x}}\bar{h})^2][\varepsilon^2\partial_{\bar{x}}\bar{w} + \partial_{\bar{z}}\bar{u}] - 4\varepsilon^2(\partial_{\bar{x}}\bar{h})(\partial_{\bar{x}}\bar{u}) = 0. \tag{19}$$

Next, we seek the solution of the governing Eqs. (14)–(19) as a perturbation series in powers of the small parameter ε, as follows:

$$\bar{u} = \bar{u}_0 + \varepsilon\bar{u}_1 + \varepsilon^2\bar{u}_2 + \cdots, \tag{20}$$

$$\bar{w} = \bar{w}_0 + \varepsilon\bar{w}_1 + \varepsilon^2\bar{w}_2 + \cdots, \tag{21}$$

$$\bar{p} = \bar{p}_0 + \varepsilon\bar{p}_1 + \varepsilon^2\bar{p}_2 + \cdots. \tag{22}$$

The lubrication approximation of the dimensionless governing equations is obtained by letting Re $\sim \mathcal{O}(1)$ and $\varepsilon \to 0$. In this context, an important consideration is made in Eq. (15a). We assume Ca $\sim O(\varepsilon^3)$ to retain the pressure term at the resulting leading order; thus, the capillary and viscous effects in our thin-film approach possess the same importance. Because of these assumptions, at the leading order in ε, the governing system adopts the following form (note that, for simplicity, we have omitted the subscript 0 in $\bar{u}_0$, $\bar{w}_0$, and $\bar{p}_0$),

$$\partial_{\bar{x}}\bar{u} + \partial_{\bar{z}}\bar{w} = 0, \tag{23}$$

$$\partial_{\bar{x}}\bar{p} = \partial_{\bar{z}}^2 u \tag{24a}$$

$$\partial_{\bar{z}}\bar{p} = 0. \tag{24b}$$

The following boundary conditions at $\bar{z} = 0$ are

$$\bar{w} = 0 \quad \text{and} \quad \bar{u} - \beta_0\partial_{\bar{z}}\bar{u} = 0. \tag{25}$$

The boundary conditions at the interface Eqs. (17)–(19), at $\bar{z} = \bar{h}(\bar{x}, \bar{t})$, are

$$\partial_{\bar{t}}\bar{h} + \bar{u}\,\partial_{\bar{x}}\bar{h} = \bar{w}, \tag{26}$$

$$\bar{p} + \bar{\Pi}_{ac} = -\partial_{\bar{x}}^2\bar{h}, \tag{27}$$

$$\partial_{\bar{z}}\bar{u} = 0. \tag{28}$$

Let us note that the spatiotemporal function, $\bar{\Pi}_{\text{ac}} = \bar{\Pi}_{\text{ac}}(\bar{x}, \bar{t})$ introduced on Eqs. (18) and (27) constitutes a *dimensionless acoustic pressure*, defined by

$$\bar{\Pi}_{\text{ac}} = 2\,\mathcal{C}\sin(2\bar{\kappa}\bar{x})\cos(2\bar{\Omega}\bar{t}), \tag{29}$$

which has been obtained by substituting a dimensionless pressure $\bar{\Pi}_{\text{ac}} = \Pi_{\text{ac}}L/\varepsilon\sigma$, a dimensionless frequency $\bar{\Omega} = \Omega L/U$ and a dimensionless wave number $\bar{\kappa} = \kappa L = 2\pi L/\lambda$ into Eq. (10). In this context, we note that the quantity L/U is the *viscous-capillary time scale* [18] and λ is the SAW wavelength. Thus, Eq. (29) depicts a standing wave in terms of a dimensionless wave number, $\bar{k}$, a dimensionless frequency, $\bar{\Omega}$, and an *acoustic capillary number*, $\mathcal{C}$. The latter is defined by

$$\mathcal{C} \equiv \frac{\rho\Omega^2 A^2 H\cos^2\theta_R}{\varepsilon^2\sigma}. \tag{30}$$

Inversely proportional to the square of the aspect ratio ε, this dimensionless quantity measures the importance of the acoustic stress relative to the drop's resistance to be deformed, i.e., the capillary stress. We note that θ_R is the *Rayleigh angle*, a quantity which considers the acoustic propagation properties of the drop-substrate system, as referred to before.

Let us now focus our attention on Eq. (24b), such expression indicates that the pressure is not a function of $\bar{z}$; therefore, Eq. (24a) is integrated twice, yielding the velocity profile in the form

$$\bar{u} = \partial_{\bar{x}}\bar{p}\left(\tfrac{1}{2}\bar{z}^2 - \bar{h}\bar{z} - \beta_0\bar{h}\right). \tag{31}$$

Here, the constants of integration were determined by considering the Navier slip model at $\bar{z} = 0$ and the tangential stress condition at $\bar{z} = \bar{h}(\bar{x}, \bar{t})$, given by Eqs. (25) and (28), respectively. Integration of Eq. (23) in $\bar{z}$ results in the following equation:

$$\int_0^{\bar{h}} \partial_{\bar{x}}\bar{u}\,d\bar{z} + \bar{w}|_0^{\bar{h}} = 0. \tag{32}$$

Applying the Leibnitz rule to Eq. (32) and combining with the boundary condition Eq. (26) and $\bar{w} = 0$ at $\bar{z} = 0$, then, Eq. (32) is rewritten as follows:

$$\partial_{\bar{t}}\bar{h} + \partial_{\bar{x}}\left(\int_0^{\bar{h}} \bar{u}\,d\bar{z}\right) = 0. \tag{33}$$

Substituting the velocity profile Eq. (31) into Eq. (33), we obtain the partial differential equation that allows determining the film thickness $\bar{h}$,

$$\partial_{\bar{t}}\bar{h} - \partial_{\bar{x}}\left[\partial_{\bar{x}}\bar{p}\left(\tfrac{1}{3}\bar{h}^3 + \beta_0\bar{h}^2\right)\right] = 0. \tag{34}$$

Combining Eqs. (27) and (29), we can express the hydrodynamic pressure $\bar{p}$ in terms of the acoustic capillary number, in the form

$$\bar{p} = -\partial_{\bar{x}}^2\bar{h} - 2\,\mathcal{C}\sin\left(2\bar{\kappa}\bar{x}\right)\cos\left(2\bar{\Omega}\bar{t}\right). \tag{35}$$

Equation (34) constitutes an evolution equation in time and space for the destabilization mechanism at the drop's air-liquid interface under the influence of the Navier slip condition and acoustic excitation via SAWs. When the slip coefficient is zero, we recover the evolution equation derived by Qi *et al.* [18] under the classical no-slip condition at the solid wall. The solution of Eq. (34) will allow to obtain fundamental information about the formation of capillary waves at the drop's free surface. Specifically, by analyzing such deformations, important parameters regarding SAW atomization, like the *instability threshold* and *viscous-capillary resonant frequency* [18], will be determined and evaluated in the context of slippage phenomenon at the solid wall.

Equation (34) requires one initial condition and four boundary conditions. We can appreciate the above if we replace Eq. (35) into Eq. (34). In this manner, we obtain a four-order partial differential equation for the thickness h. An important aspect worthy of consideration during the choice of the initial condition for Eq. (34) consists in the definition of the proper geometry which approximates the drop in an undeformed state, without the influence of any acoustic stress and with a contact angle beneath $90°$. Thus, the air-liquid interface at $\bar{t} = 0$ is conveniently approximated by a Gaussian profile in the form

$$\bar{h}(\bar{x}, \bar{t} = 0) = \exp\left(-\frac{\bar{x}^2}{0.05}\right). \tag{36}$$

The following symmetry conditions are subsequently imposed at the left and right boundaries of the spatial domain:

$$\partial_{\bar{x}}\bar{h}(\bar{x}, \bar{t})|_{\bar{x}\to\pm\infty} = 0, \tag{37}$$

and

$$\partial_{\bar{x}}^3 \bar{h}(\bar{x}, \bar{t})|_{\bar{x} \to \pm \infty} = 0. \tag{38}$$

Although Eq. (34) refers to the leading order of the lubrication theory of Eqs. (17) and (18), it does not admit an analytical solution due to the presence of strong nonlinearities and higher-order spatial derivatives. Therefore, Eq. (34), subject to the acoustic forcing Eq. (35) and auxiliary condition Eqs. (36)–(38), is solved numerically by the *method of lines* (MOL) [55,56]; a deep insight regarding the implementation of such a method is shown in the Appendix.

The implementation of MOL demands a series of parameters—regarding the drop physical and geometrical properties—to be precisely defined. In this context, a clear knowledge of the typical values associated with acoustic excitation via SAWs (operational frequencies and wavelengths besides wave amplitudes) is needed to build a well-grounded estimation of the acoustic capillary number. Of course, a proper estimation of the characteristic velocity of the flow field, besides the dimensionless frequency and wave number, is essential to provide a feasible representation of the effects caused by the acoustic stress at the free surface of our numerical drop model. Thus, we proceed to show the values and orders of magnitude of those parameters of fundamental relevance for the numerical solution of Eq. (34).

We consider water properties at standard room temperature with $\rho = 1000$ kg/m^3, $\mu = 1.0 \times 10^{-3}$ kg/m s, and $\sigma = 72.8$ mN/m. The speed of sound in water $v_f \approx 1482.5$ m/s is used to estimate the acoustic radiation leakage effect, as explained below. Because of the lubrication-type approach, a slender drop with length $L(\text{m}) \sim 10^{-4}$–10^{-3} and height $H(\text{m}) \sim 10^{-5}$–10^{-4} has been considered, such that $\varepsilon \ll 1$. The characteristic velocity of the fluid is $U(\text{m/s}) \sim \sigma \varepsilon^2 / \mu \sim 10^{-2} - 1$. Such velocity, in conjunction with our estimation for L, yields a characteristic time $t_c(\text{s}) \sim L/U \sim 10^{-4} - 10^{-3}$, which agrees with the previously reported temporal scale governing the deformation of the air-liquid interface [18]. Next, we address the parameters associated with the acoustic pressure Π_{ac}, defined at Eq. (10). We consider a linear excitation frequency f_e on the order $\sim 10^7$ Hz [15,16,20–22,31,57], then, the angular excitation frequency (given by $\Omega = 2\pi f_e$) is on the order 10^8 rad/s. Moreover, we consider typical SAW wavelengths and amplitudes with $\lambda(\text{m}) \sim 10^{-4}$ and $A(\text{m}) \sim 10^{-9}$, respectively. Addressing now the parameters belonging the dimensionless acoustic pressure at Eq. (29), it results that the considerations given above yield $\bar{\Omega} \sim \mathcal{O}(10^4)$ and $\bar{\kappa} \sim \mathcal{O}(10)$.

The estimation of the acoustic capillary number requires to take into account the diffraction phenomenon of the SAW traveling across the substrate into the water drop. Such phenomenon is quantified by the Rayleigh angle, θ_R, defined by $\theta_R = \arcsin(vf/vs)$, where v_f and v_s represent the wave propagation speed across the water drop and the substrate, respectively. Specifically, our study considers $\theta_R \approx 22°$, with $v_f \approx 1482.5$ m/s and $v_s \approx 3965.0$ m/s; the latter being the SAW propagation speed across lithium niobate, broadly employed on the fabrication of piezoelectric substrates. In view of the above, we consider $\cos^2 \theta_R \sim \mathcal{O}(1)$.

Finally, we address the dimensionless slip coefficient, β_0, employed during our numerical simulations, which is given by $\beta_0 = \beta/H$ and relates the Navier slip-length and the characteristic height of the drop. As our numerical model portrays a drop-substrate system with a contact angle below $\theta_c < 90°$, we have taken into account empirical slip lengths measurements in systems with complete [35–38] and partial [39–46] wetting which report $10^{-9} \leqslant \beta(\text{m}) \leqslant 10^{-6}$; thus, in view of the scale length for H provided above, we have $\beta_0 \sim \mathcal{O}(10^{-2}$–$10^{-1})$. Once all the essential parameters for our numerical study have been defined, we proceed to analyze the output obtained by the implementation of MOL (see the Appendix) in the results and discussion in Sec. III.

III. RESULTS AND DISCUSSION

The numerical output obtained from MOL consists in the film thickness $\bar{h}(\bar{x}, \bar{t})$ and can be visualized either as a *surface* defined on the coordinate space $(\bar{x}, \bar{z}, \bar{t})$ by the function $\bar{z} \equiv \bar{h}(\bar{x}, \bar{t})$ or as a component of a *scalar function* $F(\bar{\mathbf{x}}, \bar{t})$, which describes the interface shape in the sense
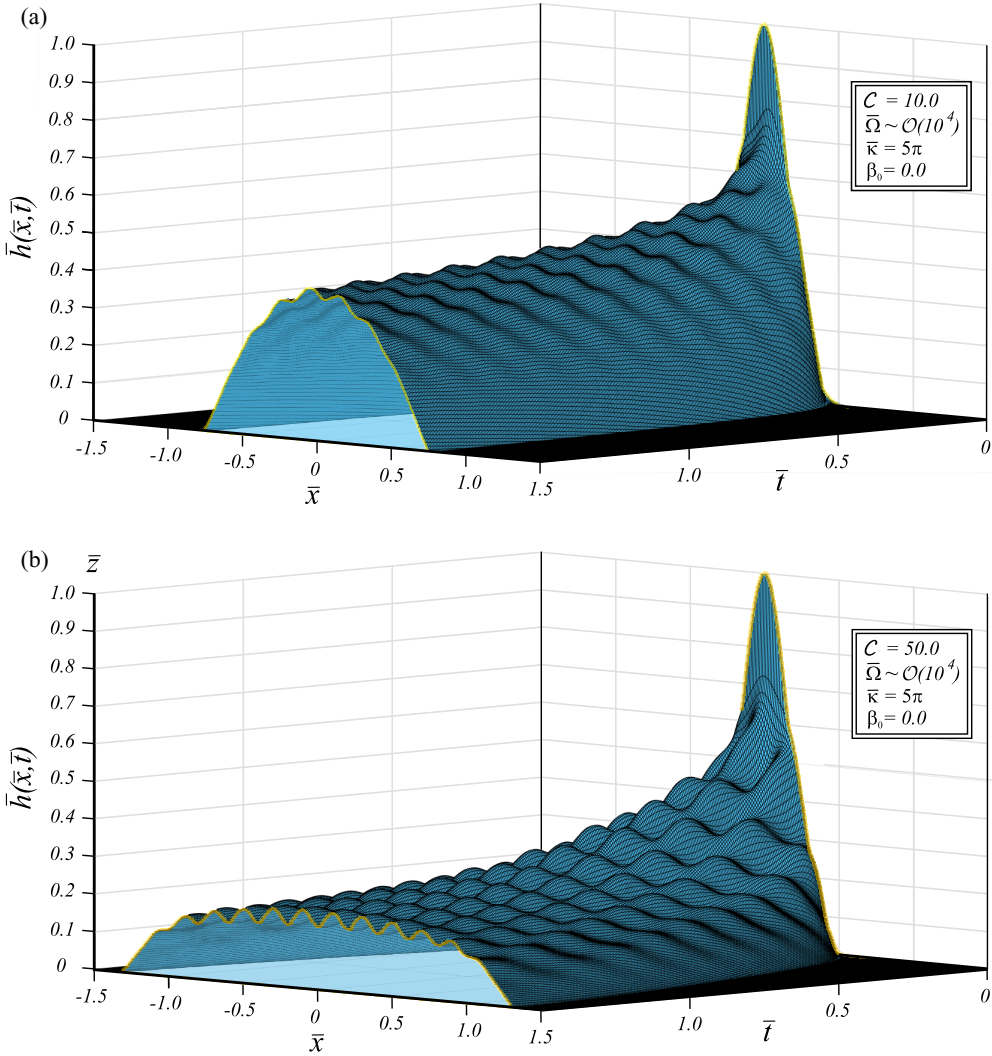
(a)

(b)

FIG. 2. Spatiotemporal evolution surface F that depicts the deformation process of a single drop profile along the dimensionless time $\bar{t}$. Case (a) shows a stress ratio quantified at $\mathcal{C} = 10.0$ and results in a quasistable deformation process that keeps away the drop of being atomized, i.e., acoustic forcing is nearly balanced respect capillary forces at the interface. However, case (b) with $\mathcal{C} = 50.0$, suggests a strong dominance of the acoustic stress over the surface tension stabilizing effect that results in a drop profile susceptible to be atomized.

that the interface is the set of points $\bar{\mathbf{x}} = (\bar{x}, \bar{z})$, such that $F(\bar{\mathbf{x}}, \bar{t}) \equiv 0$. Then, by combining both definitions, the following equation of a surface is obtained:

$$F(\bar{\mathbf{x}}, \bar{t}) \equiv \bar{h}(\bar{x}, \bar{t}) - \bar{z} \equiv 0. \qquad (39)$$

We begin our discussion by presenting the MOL output as a scalar function F subject to Eq. (39), as can be observed in Fig. 2. In this context, let us note that we focus our attention on illustrating in first place the key role acoustic capillary number plays on the the formation of capillary waves via SAWs; after that, we analyze the influence of slippage phenomenon on SAW atomization. Accordingly, Fig. 2 portrays the response of an air-liquid interface toward an acoustic stress in the absence of

slippage at the wall, under the influence of $\mathcal{C} = 10$ [Fig. 2(a)] and $\mathcal{C} = 50$ [Fig. 2(b)]. The acoustic forcing exerted on the free surface was defined at Eq. (29) and depends on the dimensionless frequency ($\bar{\Omega}$) and wave number ($\bar{\kappa}$) besides the acoustic capillary number. The surface F has been plotted in a time interval $0 \leqslant \bar{t} \leqslant 1.5$ and over a spatial domain $-1.5 \leqslant \bar{x} \leqslant 1.5$ with $\bar{\Omega} = 10^4$ and $\bar{\kappa} \sim \mathcal{O}(10)$. The cross-sections obtained when F intersects a temporal plane (parallel to the $\bar{x}\bar{z}$ plane), constitutes the *drop profiles* at a particular time, $\bar{t}$.

As can be observed in Figs. 2(a) and 2(b) the simulation starts with the Gaussian profile defined by Eq. (36); this profile approximates the drop's interface in an undeformed state, as a continuous liquid film with a contact angle below $90°$. We note that the interface of the liquid film experiences an initial "transient," within $\bar{t} < 0.18$, characterized by a sudden reduction in the aspect ratio, ε, with strongly marked curvature gradients at the drop's interface, as shown in Fig. 2. However, a feasible representation of the free surface physical response only begins once the interface finds its *equilibrium position* at $\bar{t} \approx 0.18$. Specifically, during such equilibrium configuration, the drop profile adopts a configuration which resembles a *dome*, i.e., a concave shape with subtle deformations along the free surface [e.g., see Figs. 3(a-i), 3(b-i), and 3(c-i) portrays three equilibrium configurations under three values for $\mathcal{C}$]. Once the initial transient has died out and the equilibrium position of the free surface has been reached, a series of ripples are developed on the drop's interface for $\bar{t} > 0.18$. Such structures, also called *capillary waves*, harmonically oscillate on the free surface as an interfacial standing wave with a frequency that is know as the *capillary resonance frequency* and possess also an amplitude which depends on the acoustic capillary number, as explained below.

The amplitude of the capillary waves developed at the interface can be interpreted as an indicative of the drop's resistance to being deformed by the acoustic stress. In this context, Fig. 2(a) shows that a water drop under the influence of a stress ratio quantified by $\mathcal{C} = 10$ develops a series of subtle capillary waves along the free surface and adopts a concave shape that practically remains unaltered along time. Such geometry indicates the drop is very close to an equilibrium configuration, thus, the capillary stresses acting over the free surface are sufficiently strong to prevent the development of the excessively elongated capillary waves needed for interfacial breakup and drop's atomization. However, Fig. 2(b), with $\mathcal{C} = 50$, shows a case at which the acoustic pressure gains more relevance than the capillary forces at the interface, deriving in the formation of excessively elongated capillary waves with abrupt curvature gradients. As discussed in detail later, the amplitude of some of the induced capillary waves in Fig. 2(b) has achieved a critical value called *instability length*; thus, atomization induced via SAWs is feasible.

Let us note that the numerical simulations depicted in Figs. 2(a) and 2(b) indicate that to promote a significant deformation of the air-liquid interface, an stress ratio with $\mathcal{C} \sim \mathcal{O}(10)$ is required. The feasibility of such order of magnitude can be demonstrated by substituting the drop's parameters listed at Sec. II into Eq. (30). In this context, we also note that the magnitude of $\mathcal{C}$ differs considerably from its viscous counterpart, i.e., the capillary number Ca (usually, Ca $\ll 1$). The aspect ratio considered during our lubrication-type approach, $\varepsilon \ll 1$, plays a key role at such magnitude difference. While the capillary number has been scaled as Ca $\sim \varepsilon^3$, the acoustic capillary number, in contrast, is in inverse proportion respect ε [see Eq. (30)]. Such aspect ratio dependence contributes also to explain the magnitude of $\mathcal{C}$ shown at our numerical results.

Continuing with the analysis of Fig. 2, a *spreading effect* can be observed on the free surface, which is deeply associated with the acoustic forcing irradiation on the air-liquid interface. The spreading phenomenon implies a reduction in the drop's aspect ratio, ε, as time progresses, i.e., a gradual decrease in the film height (H) in conjunction with an increment at the film length (L). We note the drop spreading is stronger as the acoustic capillary number varies from 50.0 to 10.0. Thus, Fig. 2(a) shows an air-liquid interface with a greater resistance against spreading than the free surface depicted in Fig. 2(b), as a consequence, the drop thickness is expected to decay at a faster rate as $\mathcal{C} \rightarrow 50.0$. The decrease of the aspect ratio for a drop exposed to SAW excitation has already been experimentally documented [18], in this context, the numerical output presented in Fig. 2 confirms such phenomenon and illustrates that the aspect ratio drop depends on the competence between acoustic and capillary stresses quantified by $\mathcal{C}$.
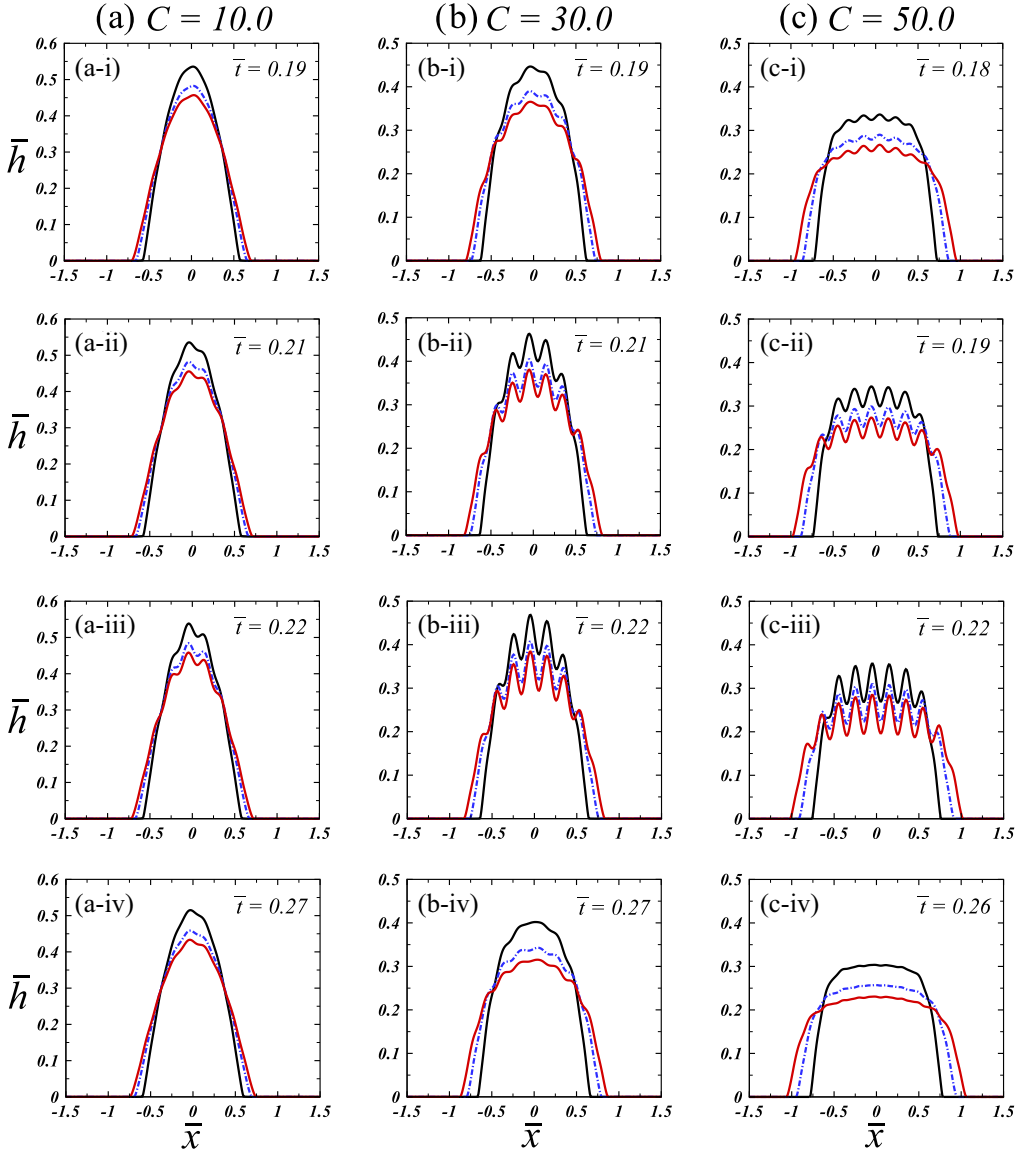
FIG. 3. Spatiotemporal evolution of an air-liquid interface subjected to SAW excitation, in terms of $\bar{h} = h(\bar{x}, \bar{t})$. Three values of $\mathcal{C}$ are considered (10.0, 30.0, 50.0), distributed in three columns (a)–(c). Each column contains a sequence of four subfigures (i)–(iv), portraying the first cycle of the induced standing wave at the free surface. In this context, each subfigure shows three drop profiles developed under a particular slip coefficient: ——$\beta_0 = 0.0$, - - - $\beta_0 = 0.05$, and —— $\beta_0 = 0.1$. All of the profiles have been obtained under an acoustic excitation with $\bar{\Omega} = 10^4$ and $\bar{\kappa} \sim \mathcal{O}(10)$ (see Sec. II).

Slippage at the solid-liquid interface is closely related to the interfacial spreading phenomenon described above. To deliver a comprehensive analysis of such relationship, we make use of a two-dimensional representation of the surface F by plotting its intersection with different temporal planes worth of interest, considering in the process both, the absence and presence of slippage at the wall besides several values of the acoustic capillary number. Accordingly, various drop profiles are shown on Fig. 3, distributed in an "array" consisting of three columns and four rows. Each

column corresponds to a specific value of $\mathcal{C}$ (10, 30, and 50) and is composed of four cases [(i)–(iv)], which portray the film evolution at different times $\bar{t}$. In this context, we note that each element or "panel" in Fig. 3 depicts three drop profiles developed under the influence of an acoustic forcing with a dimensionless frequency $\bar{\Omega} = 10^4$ and a wave number $\bar{\kappa} \sim \mathcal{O}(10)$. Moreover, each drop profile has been developed under the influence of a particular value of the slip coefficient, i.e., $\beta_0 = 0.0$, 0.05, and 0.1. Cases (i)–(iv) in each column shown in Fig. 3 portray the first cycle of the standing wave developed at the air-liquid interface, consisting in the film evolution from an equilibrium shape toward a state of maximum deformation to return, shortly after, to the equilibrium configuration. Such fundamental behavior tends to be repeated during subsequent cycles as the drop experiments the spreading effect referred to before at its base, near the reference level $z = 0$. Before proceeding to analyze the influence of slippage on SAW atomization, let us note the dimensionless slip coefficients employed at our numerical simulations (e.g., $\beta_0 = 0.05$, 0.1) are on the order 10^{-2}–10^{-1} such range is equivalent—in physical units—to a slip length (β) varying between $\mathcal{O}(10^{-7})$ and $\mathcal{O}(10^{-6})$ m, which is consistent with experimental measurements regarding the slip length developed under hydrophilic conditions (see Sec. II).

To illustrate the slippage influence on SAW atomization, three drop profiles are presented at each individual panel appearing on Fig. 3. The dotted blue line corresponds to $\beta_0 = 0.05$ and the solid red line to $\beta_0 = 0.1$. The solid black line represents the case with the no-slip condition, $\beta_0 = 0$. Let us start by analyzing the plots depicted in Fig. 3(a), which corresponds to the case $\mathcal{C} = 10$. Figure 3(a-i) shows three drop profiles at an equilibrium configuration, which is achieved immediately after the initial transient of our numerical simulation has passed away. Figure 3(a-ii) shows that, after a short time interval, a series of small-amplitude capillary waves are developed at the upper part of the free surface as a result of the exerted acoustic stress. The maximum amplitude achieved by the capillary waves is shown in Fig. 3(a-iii), nevertheless, we note that those structures are very similar to the case in Fig. 3(a-ii). Finally, at the end of the cycle, the drop profiles return to their equilibrium configuration [Fig. 3(a-iv)]. From the above sequence of events, we note that as $\beta_0 \to 0.1$, the drop height is reduced; in this context, the mass conservation principle governing the drop evolution compensates such reduction at the film thickness, $\bar{h}$, with a spreading of the drop profile along the reference level $\bar{z} = 0$. From the sequence of events depicted at column a), we note that imposing the Navier slip condition at our lubrication model causes the drop's aspect ratio (ε) to become smaller as $\beta \to 0.1$. Worth noting is the fact that the slippage influence under an acoustic capillary number $\mathcal{C} = 10$ is constrained only to modify the drop's aspect ratio without exert any direct or noticeable repercussion on the amplitude of the capillary waves generated at the top of the drop profiles. In the proximities of $\mathcal{C} = 10$, the amplitude of those capillary waves is not sufficiently large to promote drop's atomization.

Next, we address the plots shown in column (b) of Fig. 3, which evaluates the influence of a higher capillary acoustic number ($\mathcal{C} = 30$) on the free surface evolution. We note that a constant surface tension value has been assumed during our numerical simulations, thus, increasing $\mathcal{C}$ traduces in applying a higher mechanical power on the free surface. In this context, the sequence of panels from Fig. 3(b-i)–3(b-iv) shows that an increment of the acoustic stress exerted on the drop derives in the development of a series of drop profiles with a smaller thickness, $\bar{h}$—and a smaller aspect ratio (ε)—than those shown in column (a), in the same manner as discussed on our Fig. 2 analysis. Figure 3(b-i) shows a series of drop profiles under an equilibrium configuration, i.e., domelike shapes with small-amplitude capillary waves. Figure 3(b-ii) shows that, after a time interval, $\Delta\bar{t} \approx 0.02$, the exerted acoustic stress on the free surface has the strength necessary to induce considerably elongated capillary waves along the upper region of the drop profile. By comparing the drop profiles developed under the no-slip condition, $\beta_0 = 0$ (black line), with those cases developed under $\beta_0 = 0.05$ (blue dotted line) and $\beta_0 = 0.1$ (red line) at Fig. 3(b-ii), we observe that by increasing the slip coefficient, the drop spreading becomes accentuated in the same manner as explained above [case $\mathcal{C} = 10$]. Because of the considerable elongation of some of the capillary waves shown in Fig. 3(b-ii), it is more appropriated to refer them as *liquid threads*. Those structures are commonly characterized by the parameter known as the *capillary height l*, i.e., the

amplitude of the capillary structures developed on the surface of a liquid drop exposed to SAW atomization. During our study we denote the dimensionless capillary length as $\bar{l}$.

The dimensionless maximum amplitude, $\bar{l}_{\max}$, achieved by the liquid threads under $\mathcal{C} = 30$ is depicted in Fig. 3(b-iii), which suggest that $\bar{l}_{\max} \sim \mathcal{O}(10^{-1})$. Moreover, taking into account the drop dimensions previously defined on Sec. II, we note the maximum amplitude corresponds to $l_{\max}(m) \sim 10^{-5}$, in physical units. Figure 3(b-iii) also shows that—under the same acoustic capillary number— slippage (red lines) favors the formation of additional liquid threads at the drop's free surface respect the classical no-slip condition (black lines). Finally, Fig. 3(b-iv) shows a series drop profiles under the equilibrium configuration once the excessive elongations have taken place. Let us recall that the thickness, $\bar{h}$, exhibited by the drop profiles at the end of the cycle is not the same as the beginning, there is a continuous decay at ε as the temporal scale, $\bar{t}$, progresses.

Next, a few considerations are made to determine if the liquid threads shown in Fig. 3(b-iii) indicate an imminent interfacial destabilization and therefore the atomization of the air-liquid interface. We note that our lubrication-type approach has resulted in the development of a drop model unable to portray the rupture mechanism of the liquid threads which precedes the generation of aerosol droplets, thus, to predict the rupture of the liquid threads we make use of a parameter which magnitude can be used as an indicative of the imminent drop's atomization: the *instability length*, denoted at our study as l_{inst}. The importance of such parameter for our study can be explained by bringing into consideration the physical background behind the drainage and rupture of the liquid threads leading toward SAW atomization. In this context, let us consider an imaginary air-liquid interface under SAW excitation and let us proceed to divide it into a series of very small segments, each one of them governed by the normal stress balance $(p + \Pi_{\mathrm{ac}}) - p_{\mathrm{atm}} = -\sigma \partial_x^2 h$. This balance indicates that, for a given surface tension value, the curvature of each segment depends on the pressure jump across the interface. As the exerted acoustic stress, Π_{ac}, varies across time and space, it is expected the curvature of our interfacial segments not to remain constant along the free surface; in this case, it is said there are *curvature gradients* developed along the free surface which are manifested in the form of capillary waves. In view of the above, the formation of capillary waves can be associated with the presence of pressure imbalances along the free surface, specifically, their "throughs" are regions of maximum pressure on the interface while their "crests" constitutes regions where the pressure is minimum. Moreover, the pressure imbalances on the free surface induces a fluid motion along each one of the capillary waves. Such localized fluid motion is responsible of the gradual elongation in the capillary waves, as shown in Figs. 3(b-i) and 3(b-ii), and it derives in the formation of liquid threads, plotted in Fig. 3(b-iii).

As said before, the capillary length (l) measures the elongation of the liquid threads. In this context, it has been demonstrated experimentally [18] that, when the capillary length achieves a critical value—known as the instability length—the localized fluid motion at the capillary waves is so strong that leads to the *destabilization of the interface*, i.e., the imminent pinch-off of the liquid threads at their base which derives in the generation of multiple small droplets being ejected from the parent drop. Thus, to predict the presence of the destabilization phenomenon at our simplified model, we must turn our attention to the elongations developed at the capillary waves and determine if these deformations are comparable respect a given prediction of the instability length. An estimation of such critical parameter can be obtained by executing a balance between the capillary and inertial stresses acting at the air-liquid interface, however, such balance cannot be obtained from our lubrication-type approach as the inertial terms have been discarded at our asymptotic approximation of the drop's governing equations. Thus, we consider the scaling theory developed by Qi *et al.* [18], which have delivered an estimation of the critical capillary height at which the pinch-off process of the liquid threads occurs. In this context, Qi *et al.* establishes: $l_{\mathrm{inst}}(m) \sim (\rho U^2 L^3 / \sigma)^{1/2} \sim \mathcal{O}(10^{-5})$. Now, let us nondimensionalize the quantity l_{inst} by employing the characteristic height of our drop model [$H(m) \sim 10^{-5} - 10^{-4}$], yielding, $\bar{l}_{\mathrm{inst}} \sim \mathcal{O}(10^{-1} - 1)$. By comparing this order of magnitude with the liquid threads shown in Fig. 3(b-iii), is not unreasonable to assume such panel depict a series of drops at the onset of atomization, in view that the maximum capillary length exhibited by the liquid threads in all cases is on the order 10^{-1}.

At this point, we note that during our numerical simulations at least an acoustic capillary number around 30 was needed to overcome the restoring effect produced by the capillary stresses acting at the free surface of our drop model; an effect which tend to keep the drop near its equilibrium configuration at all times, as shown in column (a) of Fig. 3. In this sense, we say that $\mathcal{C} \approx 30$ determines quantitatively the existence of a critical point, known as the *instability threshold*, which indicates the minimal acoustic stress, given a fixed surface tension value, required for an air-liquid interface to achieve atomization under the influence of the standing SAW given by Eq. (29). From the results depicted in column (b), we note that the capillary length does not seem to be dependent of the slip coefficient β_0, then, slippage at the wall is not connected with the instability threshold, in other words, a drop deposited over a substrate with slippage at the wall achieves the instability threshold at the same critical stress ratio as a drop under the no-slip condition.

Increasing the stress ratio beyond the instability threshold can positively influence the aerosol generation process described before. To demonstrate this assertion, let us analyze the drop profiles depicted in column (c) of Fig. 3. Figures 3(c-i)–3(c-iv) portray the first cycle of the standing wave generated at the free surface under $\mathcal{C} = 50$. Starting from an equilibrium configuration depicted in Fig. 3(c-i), three drop profiles, developed under different sip coefficients, rapidly develop several capillary waves at their crest, as shown in Fig. 3(c-ii). Moreover, such induced capillary waves achieve a maximum elongation in Fig. 3(c-iii) with $\bar{l}_{\max} \sim \mathcal{O}(10^{-1})$. Such elongation fits into the range estimated previously for $\bar{l}_{\text{inst}}$. Thus, Fig. 3(c-iii) depicts three drop profiles at which interfacial breakup and atomization is feasible. Finally, the series of drop profiles return to the equilibrium configuration, as shown on Fig. 3(c-iv). Now, let us compare the state of maximum elongation depicted in Fig. 3(c-iii) with its counterpart in Fig. 3(b), i.e., Fig. 3(b-iii). In this context, it is possible to observe that varying $\mathcal{C}$ from 30 to 50 increases the number of capillary threads developed at the free surface, this situation traduces in a major number of aerosol droplets being ejected from the destabilized surface under $\mathcal{C} = 50$. As noted before, slippage phenomenon does not influence the capillary length of the liquid threads, nevertheless, Figs. 3(b-iii) and 3(c-iii) suggest that a slip length quantified by $\beta_0 = 0.05$ and $\beta_0 = 0.1$ has the capability to modify considerably the drop's aspect ratio (ε). In this context, those drop profiles developed under $\beta_0 = 0.1$ are of particular relevance in view that illustrate the development of additional capillary structures in comparison the no-slip case.

The drop profiles depicted in Fig. 3 has allowed us to obtain additional valuable parameters intervening at the deformation process of a drop exposed toward SAW atomization like the *capillary resonance frequency* and the *instability wavelength*. The first one can be defined as the frequency of the capillary waves developed at the interface due to SAW excitation, while the latter can be interpreted as the distance between crests or troughs of two successive liquid threads that have achieved the instability length. Such parameters are denoted in our study as f_c and λ_{inst}, respectively.

To estimate the capillary resonance frequency of our drop profiles, we note that the dimensionless period of our numerical simulations remains constant regardless the value of $\mathcal{C}$ and the presence or not of slippage at the wall. We note the period of the capillary waves at our numerical model is approximately 0.08, as can be verified on Fig. 3. Thus, taking into account the physical time scale employed at our numerical model (defined at Sec. II), we have that a capillary resonance frequency around 12.5 kHz is feasible. As the excitation frequency for SAW atomization is on the order 10^7 Hz, then, $f_c \ll f_e$. In this context the experimental evidence provided by Qi *et al.* [18] has demonstrated that the presence of a capillary frequency on the order 10^3-10^4 Hz constitutes an indicative of the dominance of viscous-capillary effects at the air-liquid interface over the inertial stresses.

The estimation of the instability wavelength is of sum importance in view that Qi *et al.* have demonstrated $\lambda_{\text{inst}} \sim d$, where d is the characteristic aerosol diameter. Moreover, since the experimental study developed by Li *et al.* [58], it has been demonstrated the instability wavelength is strongly linked with the SAW frequency f_e. In this context, endorsed with scaling theory, the work developed by Collins *et al.* [49] has delivered an accurate description of the relationship between

λ_{inst}, d, and f_e, given by

$$\lambda_{\text{inst}} \sim d \sim \frac{\sigma H^2 \text{We}^{2/3}}{\mu L^2 f_e}, \tag{40}$$

where We is the *acoustic Weber number*, defined by We $\equiv \rho(A\Omega)^2 L/\varepsilon\sigma$. At this point, let us note the dimensionless quantity We is analogous to the acoustic capillary number, $\mathcal{C}$, which was defined by Eq. (30). The only difference between both quantities lies in the presence of the SAW diffraction term, $\cos^2 \theta_R$. Nevertheless, we note that $\cos^2 \theta_R \sim \mathcal{O}(1)$, then, we can assert that $\mathcal{C} \sim$ We. Thus, by substituting at Eq. (40) the orders of magnitude regarding the geometrical and physical drop properties—all of them previously defined on Sec. II— and taking into account that f_e(Hz) $\sim 10^7$ and $\mathcal{C}^{2/3} \sim \mathcal{O}(10)$, we have λ_{inst}(m) $\sim 10^{-6}$. Now, let us turn our attention into Fig. 3, specifically Figs. 3(b-iii) and 3(c-iii), to graphically estimate the instability wavelength of our drop profiles. In this context, the dimensionless instability wavelength is estimated as $\bar{\lambda}_{\text{inst}} \sim \mathcal{O}(10^{-1})$ with and without the presence of slippage. In physical units, such value corresponds to λ_{inst}(m) $\sim 10^{-6}$–10^{-5}, which agrees with the theoretical prediction provided by Eq. (40). As $d \sim \lambda_{\text{inst}}$, it is possible to assert that the breakup of the liquid threads exhibited in Fig. 3 derives in the generation of aerosol with a characteristic diameter d(m) $\sim 10^{-6}$–10^{-5}.

A. Slippage influence on the aspect ratio of a drop exposed to SAW atomization

As mentioned before, the imposed standing acoustic pressure ($\bar{\Pi}_{\text{ac}}$) on our drop model promotes the development of a corresponding standing wave on the free surface. The first cycle of such wave was discussed on our Fig. 3 analysis. Once the first cycle finishes, a similar sequence of deformation events follows on, i.e., drop profiles oscillating between configurations of maximum and minimum elongation. Nevertheless, the aspect ratio of the drop decreases as time progresses and context, slippage at the wall enhances the drop spreading and Fig. 4 confirms such assertion. Specifically, Fig. 4 show nine panels distributed throughout three columns under different values of $\mathcal{C}$ (10,30, and 50). Each panel portrays drop profiles developed under different slip coefficients ($\beta_0 = 0.0, 0.05, 0.1$). The sequence of events (i–iii) portrays now the drop response at different times ($\bar{t}$), in this context, the influence of slippage is evident at the drop spreading, specially beyond the critical acoustic capillary number $\mathcal{C} = 30$. Moreover, the results depicted in columns (b) and (c) allows us to assert that the presence of slippage at the wall accentuates the effect the variation of the acoustic capillary number has on the drop's aspect ratio during SAW atomization process. In this sense, slippage at the wall under hydrophilic conditions exerts a direct repercussion on fundamental aspects usually affected by the mechanical power exerted on the fluid drop, i.e., the aspect ratio and the formation of liquid threads. According to the numerical output presented on Figs. 3 and 4, the thickness and length of the parent drop is affected by the presence of slippage phenomenon, thus, $\varepsilon = \varepsilon(\beta_0)$. However, the estimation provided by Collins *et al.* [see Eq.(40)] shows the droplet diameter, d, depends on the quantity $\varepsilon^2 \equiv H^2/L^2$. Thus, our study focuses next in developing an analytical relationship between ε and β_0 to provide an estimation of the droplet diameter in terms of the slip coefficient. Such estimation will allow us to evaluate the influence of slippage phenomenon over a parameter of sum importance at SAW atomization: the aerosol characteristic diameter d.

To determine the relationship between ε and β_0, we have made use of the numerical drop model described throughout Figs. 2, 3, and 4 and estimated the aspect ratio temporal evolution under different slip coefficients and acoustic capillary numbers. The results are shown in Fig. 5, which depict two cases: $\mathcal{C} = 10.0$ [Fig. 5(a)] and $\mathcal{C} = 50.0$ [Fig. 5(b)]. In both cases, the numerical estimation of $\varepsilon(\bar{t})$ under different slip coefficients ($\beta_0 = 0.0, 0.05, 0.1$, and 0.2) has been plotted using square symbols whereas continuous lines of different colors are used to describe the regression fit of our numerical estimations. Such regression fit has been implemented to obtain an analytical description of the dependence between ε and $\bar{t}$. In this context, we note that the temporal evolution of the aspect ratio can be approximated as $\varepsilon = B\bar{t}^n$, i.e., a power-law relationship, where B and n are constants which depend on the slip coefficient β_0.
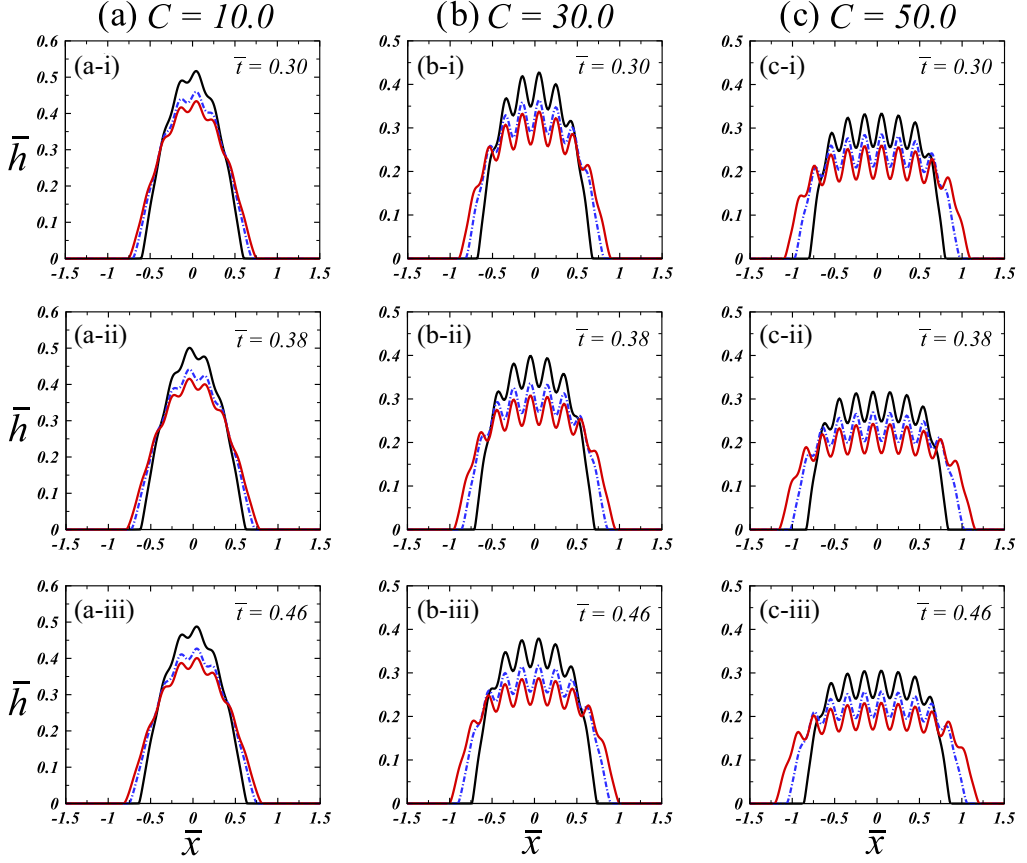
FIG. 4. Spatiotemporal evolution of an air-liquid interface subjected to SAW excitation, in terms of $\bar{h} = h(x, \bar{t})$. Three values of $\mathcal{C}$ are considered (10.0, 30.0, 50.0), distributed in three columns (a), (b), (c). Each column contains a sequence of three subfigures (i)–(iii), portraying the influence of slippage phenomenon at the drop's aspect ratio, ε. In this context, each subfigure shows three drop profiles developed under a particular slip coefficient: —— $\beta_0 = 0.0$, - - - $\beta_0 = 0.05$ and —— $\beta_0 = 0.1$. All the drop shapes have been obtained under an acoustic excitation with $\bar{\Omega} = 10^4$ and $\bar{\kappa} \sim \mathcal{O}(10)$.

Let us note that the curve $\varepsilon(\bar{t})$ developed under $\mathcal{C} = 10$ with $\beta_0 = 0.0$ in Fig. 5(a) exhibits the formation a small plateau for $0 \leqslant \bar{t} \lesssim 2$ [see also inset **A** in Fig. 5(a)]. Such flat region precedes the nonlinear decay of the aspect ratio under the no-slip condition in the form $\varepsilon = 0.2\bar{t}^{-0.3}$. Moreover, Fig. 5(a) shows that keeping $\mathcal{C}$ fixed at 10.0 and varying the slip length from 0 to 0.05 causes the evolution of the aspect ratio to be significantly affected. In this context, the plateau formed during the no-slip condition vanishes, and the regression coefficients B and n of the power-law relationship between ε and $\bar{t}$ decreases in magnitude, which traduces in smaller values of the aspect ratio being achieved under a slip coefficient quantified by 0.05 in comparison the no-slip case. As β_0 continues increasing beyond 0.05, we note the coefficient B remains constant, however, n keeps decreasing, thus, smaller valuer of the aspect ratio are expected to be obtained as $\beta_0 \to 0.2$.

The fundamental behavior of $\varepsilon(\bar{t})$ depicted in Fig. 5(a) is repeated in Fig. 5(b); nevertheless, we note several important differences. First, the plateau which was referred to above to be developed for the no-slip condition has disappeared by varying $\mathcal{C}$ from 10 to 50. The power-law relationship governing the decrease of the aspect ratio under the presence of slippage and $\mathcal{C} = 50$ is characterized by a reduction of both coefficients, B and n. In this context, we note the rate of decay of ε at the four
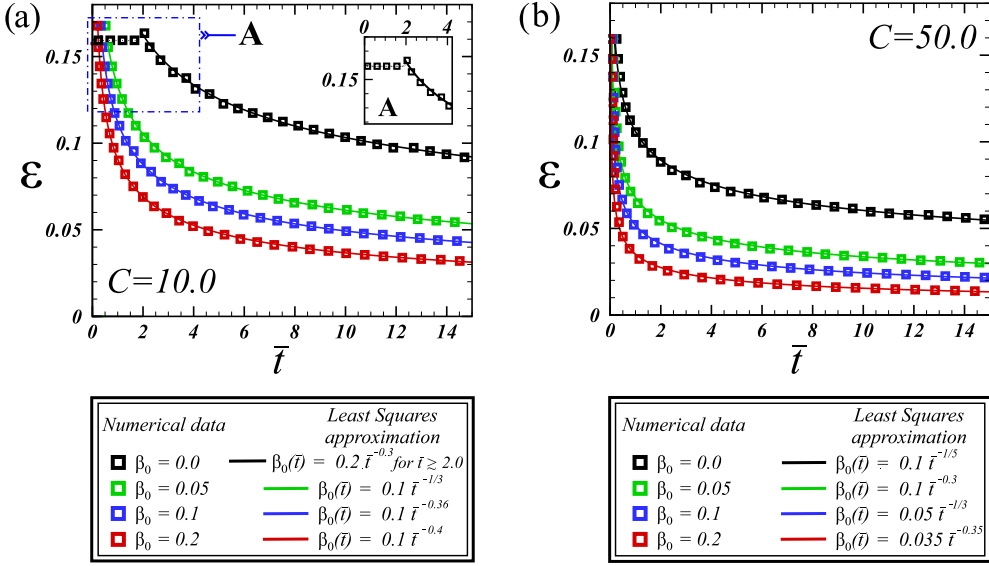
FIG. 5. Temporal evolution of the aspect ratio ε under the influence of four different slip coefficients—$\beta_0 = 0.0, 0.05, 0.1,$ and 0.2—and two particular acoustic capillary numbers: $\mathcal{C} = 10$ and $\mathcal{C} = 50$. We note panel (a) illustrates the temporal evolution of the aspect ratio obtained by keeping fixed $\mathcal{C}$ at 10 and varying the slip coefficient in the range referred to above. Moreover, panel (b) has been developed in a similar manner, however, the acoustic capillary number is now fixed at 50. On both cases, our numerical estimations have been plotted using square symbols of different colors—each color is associated with a particular slip coefficient value—whereas the continuous lines depict a regression fit of our numerical data, based on the least-squares method. In this context, a power-law relationship, in the form $\varepsilon = B\bar{t}^{\,n}$, can be used to analytically describe the dependence between ε and $\bar{t}$, except for the time interval $0 \leqslant \bar{t} \lesssim 2$ at the no-slip case depicted in panel (a). During such time interval the drop's aspect ratio results to be constant, as can be appreciated in more detail at the inset **A**. Finally, let us note that panels (a) and (b) have been developed under a dimensionless excitation frequency $\bar{\Omega} \sim \mathcal{O}(10^4)$ and a wave number $\bar{\kappa} \sim \mathcal{O}(10)$.

cases depicted in Fig. 5(b) differs substantially from their counterparts in Fig. 5(a). For example, the numerical data corresponding to the cases $\beta_0 = 0.05, 0.1,$ and 0.02 in Fig. 5(a) show an abrupt decay of the aspect ratio for $0 < \bar{t} \lesssim 6$, nevertheless, the rate of decay of $\varepsilon(\bar{t})$ varies slowly for $\bar{t} > 6$ and becomes almost zero as time progresses. However, Fig. 5(b) shows that the transition from an abrupt toward a quasisteady aspect ratio decay can occur earlier if the acoustic capillary number is increased. Accordingly, we note that, for $\bar{t} \gtrsim 4$, exists a constant rate of decay at $\varepsilon(\bar{t})$ in all the cases depicted in Fig. 5(b); such rate of decay is almost zero for the cases $\beta_0 = 0.1$ and 0.2 around $\bar{t} = 4$.

Figure 5 analysis suggests the aspect ratio of a drop exposed to SAW excitation becomes practically constant after a given time. Moreover, Fig. 5 shows that the time required for the transitory and abrupt decay of the aspect ratio to pass away depends on the acoustic capillary number. Such behavior has resulted fundamental to estimate the dependence between ε and β_0 during our study. Specifically, we have determined a function $\varepsilon = \varepsilon(\beta_0)$ by considering several evolution curves—like those depicted in Fig. 5—and choosing a sufficiently large time that assures the quasisteady evolution of ε. Subsequently, the aspect ratio values at such reference time have been plotted against the slip coefficient. In this context, let us note we have estimated $\varepsilon(\beta_0)$ at a reference time around $\bar{t} = 10$; such value constitutes a sufficiently large time beyond which is not unreasonable to assume the drop's aspect ratio remains constant, regardless the value of the acoustic capillary number. The results are depicted in Fig. 6(a), which illustrates the drop's aspect ratio as a function of the slip coefficient.
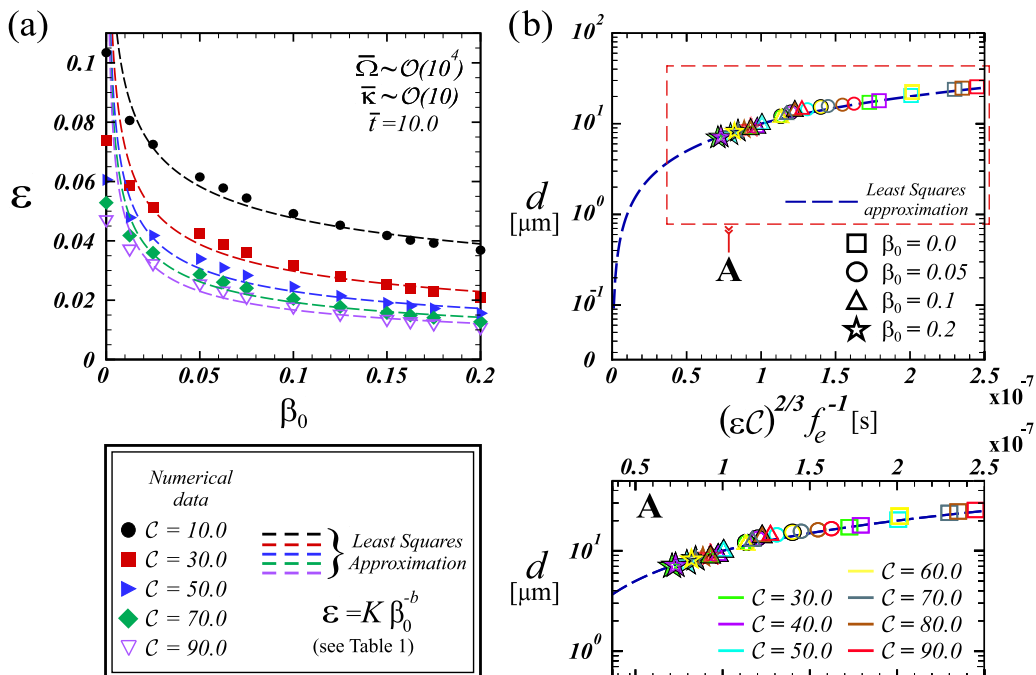
FIG. 6. The aspect ratio (ε) evolution of a drop exposed to SAW atomization against the slip coefficient (β_0) is shown in panel (a) under different acoustic capillary numbers. The numerical estimations, obtained for our drop model are represented by geometric shapes whereas the dashed lines represent a regression fit of our data. In this context we have found the relationship $\varepsilon = K\beta_0^{-b}$ for $\beta_0 \gtrsim 0.01$ (let us note the regression coefficients K and b—obtained under several acoustic capillary numbers— are specified on Table 1). Panel (b) shows several droplet diameter (d) estimations, with and without the presence of slippage, for the SAW atomization of a parent drop. Specifically, our numerical estimations for d—developed under different values for $\mathcal{C}$—are plotted as geometric shapes whereas the regression fit of our numerical data is plotted through a blue dashed line. The regression fit suggest d scales linearly respect the quantity $(\varepsilon\mathcal{C})^{2/3} f^{-1}$. Let us note the inset **A** offers a major resolution of our numerical data which have been plotted using different colors—each one of them associated to a specific value of $\mathcal{C}$— and various shapes which are related to a particular value of the slip coefficient.

Figure 6(a) shows the influence of the acoustic capillary number on the relationship $\varepsilon - \beta_0$ once the drop has achieved a quasisteady state at its geometry evolution ($\bar{t} \approx 10$). Specifically, our numerical estimation for $\varepsilon(\beta_0)$ has been plotted using different geometric shapes for five cases: $\mathcal{C} = 10, 30, 50, 70$, and 90. However, we have used a series of dashed lines of different colors to represent the regression fit of our numerical results under different acoustic capillary numbers. At this point, let us recall that the acoustic excitation implemented at our numerical simulations consists in a standing SAW with a dimensionless frequency $\bar{\Omega} \sim \mathcal{O}(10^4)$ and a dimensionless wave number $\bar{\kappa} \sim \mathcal{O}(10)$, such values, in physical units correspond to an linear excitation frequency on the order 10^7 Hz and a wavelength $\lambda(\mathrm{m}) \sim 10^{-4}$ (see Sec. II). Under such acoustic forcing our numerical study have found the onset of atomization is localized around $\mathcal{C} = 30$. In this context, Fig. 6(a) suggest that—for a fixed slip coefficient—varying $\mathcal{C}$ from 10 to 30 traduces in a substantial reduction at ε, nevertheless, we note that varying $\mathcal{C}$ at "high" values, beyond the onset of atomization, does not traduces in a significant change at ε. For example, an aspect ratio value obtained under a fixed slip coefficient and $\mathcal{C} = 70$ does not differ significantly respect its counterpart obtained under $\mathcal{C} = 90$. Moreover, the regression fit implemented under our numerical data suggest a power-law relationship

TABLE I. Least-squares approximation for numerical data depicted in Fig. 6(a).

Acoustic capillary number ($\mathcal{C}$)	$\varepsilon = K\beta_0^{-b}$
10	$\varepsilon = 0.025\beta_0^{-0.29}$
30	$\varepsilon = 0.012\beta_0^{-0.38}$
40	$\varepsilon = 0.01\beta_0^{-0.40}$
50	$\varepsilon = 0.009\beta_0^{-0.41}$
60	$\varepsilon = 0.008\beta_0^{-0.43}$
70	$\varepsilon = 0.007\beta_0^{-0.44}$
80	$\varepsilon = 0.006\beta_0^{-0.45}$
90	$\varepsilon = 0.006\beta_0^{-0.46}$

exists between ε and β_0 in the form $\varepsilon = K\beta_0^{-b}$, where K and b are constants which depend on the acoustic capillary number. Such regression coefficients are shown in Table I, which shows eight power-law expressions obtained as we varied $\mathcal{C}$ from 10 to 90 on our numerical model. Worth to be mentioned is the fact that the relationship $\varepsilon = K\beta_0^{-b}$ is applicable only for $\beta_0 \gtrsim 0.01$. In this sense, we note that Fig. 6(a) shows the aspect ratio evolution under slip coefficients below 0.01 differs considerably from the regression curve. Nevertheless, the least-squares fitting we have implemented allow us to deliver important considerations for the aspect ratio behavior under slip coefficients beyond 0.01. In this sense, let us now fix the acoustic capillary number and consider β_0 variable; the results can be visualized again in Fig. 6(a), which suggest that—given a value of $\mathcal{C}$—the range $0.1 < \beta_0 \lesssim 0.2$ does not traduces in a significant change in the drop's aspect ratio. However, the slip range $0.0 < \beta_0 \lesssim 0.1$ considerably influences the aspect ratio of a drop exposed to SAW excitation, regardless of the acoustic capillary number under consideration. Thus, we can assert a slip coefficient with $\mathcal{O}(10^{-2}) \lesssim \beta_0 \lesssim \mathcal{O}(10^{-1})$ has the potential to significantly affect the drop spreading at SAW atomization. If we consider physical units, then the above interval corresponds to slip lengths (β) on the order of 10^{-7}–10^{-6} m. Such range fits into the experimental lengths reported on specialized literature regarding slippage phenomenon [34].

As referred to before, the characteristic diameter of the droplets being ejected from the parent drop during SAW atomization (d) is predicted through Eq. (40). Let us note such expression has been developed, under the classical no-slip condition by Collins *et al.* [49] and expresses d is dependent on the aspect ratio of the parent drop (ε) and scales linearly respect the quantity $\text{We}^{2/3} f_e^{-1}$. Moreover, the results presented throughout Figs. 5 and 6(a) suggest the aspect ratio of a drop under SAW atomization is influenced by slippage at the wall, then, is expected the aerosol characteristic diameter to be also influenced by the slip coefficient. In this context, we proceed to employ the power-law relationship discussed above—i.e., $\varepsilon = K\beta_0^{-b}$—to propose an estimation of the aerosol characteristic diameter in terms of the dimensionless slip coefficient, given by

$$d \sim \frac{\sigma \left(K\beta_0^{-b} \right)^2 \mathcal{C}^{2/3}}{\mu f_e} \quad \text{for} \quad \beta_0 \gtrsim 0.01. \tag{41}$$

Several important considerations are made at this point regarding Eq. (41). In first place let us note that the acoustic Weber number, appearing originally at Eq. (40) has been replaced by the acoustic capillary number, in view that we consider $\text{We} \sim \mathcal{C}$, as explained before. Second, we note our proposed estimation for d applies for $\beta_0 \gtrsim 0.01$ in view that the curves $\varepsilon - \beta_0$ do not depict a power-law behavior for $\beta_0 \lesssim 0.01$, as explained during our analysis regarding Fig. 6(a). Finally, we note that Eq. (41) establishes d scales linearly respect $\mathcal{C}^{2/3} f_e^{-1}$.

Next, we proceed to make use our aspect ratio estimations and calculate the aerosol characteristic diameter, d, with and without the influence of slippage. In the process, the validation of our numerical model is attended by comparing the quantity d respect droplet diameters already

reported on specialized literature regarding SAW atomization. Specifically, we consider of particular relevance the diameter measurements provided by the experimental/numerical work developed by Collins *et al.* [49]. By analyzing the destabilization via SAWs of a small-scale water meniscus formed between the edge o a wetted paper wick and an rigid substrate, Collins *et al.* showed that a significant region of the meniscus evolved into a thin film during the atomization process. Such thin film region exhibited a geometrical disparity (i.e., $H \ll L$), similar to that assumed to exist at the parent drop during our lubrication type approach implemented on Sec. II. Although the work developed by Collins *et al.* did not take into account the influence of slippage phenomenon at the wall, it reports valuable data for our study. In this context, several experimental measurements were made at such study, regarding the characteristic diameter of the aerosol ejected from the thin film region under excitation via SAWs. Those measurements allowed Collins *et al.* to demonstrate that d scales linearly respect the quantity $We^{2/3} f_e^{-1}$, as Eq. (40) suggests. Thus, being aware about the presence of an important similarity between our study and the work provided by Collins *et al.*—i.e., the analysis of the destabilization mechanism at a water thin film with a geometrical disparity, exposed to a high-frequency acoustic excitation with $f_e(Hz) \sim 10^7$—we proceed to validate our drop model by considering the experimental data provided by their work.

We begin by considering the four slip cases we have used during our discussion regarding Figs. 5 and 6(a), i.e., $\beta_0 = 0.0, 0.05, 0.1$, and 0.2. For each slip case we use the data provided in Fig. 6(a) and Table I to estimate ε under seven different values of the acoustic capillary number above the onset of atomization, i.e., $\mathcal{C} = 30, 40, 50, 60, 70, 80$, and 90. Immediately after we make use of Eq. (40) or Eq. (41) to calculate d, considering, in the process, an excitation frequency $f_e \sim 10^7$ Hz. In this context, let us recall that Eq. (41) is limited for slip coefficients beyond 0.01, thus, for the case $\beta_0 = 0.0$, we apply Eq. (40) whereas for the slip cases ($\beta_0 = 0.05, 0.1, 0.2$) we use Eq. (41). Moreover, let us note that for the no-slip case we have implemented Eq. (40) in the form $d = \sigma H^2 \mathcal{C}^{2/3} / \mu L^2 f_e$ as we have considered $We \sim \mathcal{C}$. The results of such estimation are graphically depicted in Fig. 6(b), which show the aerosol characteristic diameter for a drop exposed to excitation via SAWs, under different slip coefficients at the solid wall and under various acoustic capillary numbers. We note our diameter estimations are portrayed in a similar framework to that used by Collins *et al.* [49] to depict their results [see Fig. 5(b) at such study]. Thus, we have plotted d against the quantity $(\varepsilon \mathcal{C})^{2/3} f_e$ for comparison purposes.

In Fig. 6(b), our estimation of d appears represented by various geometric shapes whereas the blue dashed lines describe a regression fit of our diameter predictions. In this context, let us note that we make use of four different geometric shapes (a rectangle, circle, triangle, and a star symbol) to denote our estimation of the droplet diameter under a specific value of the slip coefficient, however, as we are also evaluating the influence of the acoustic capillary number on d, we make use of seven different colors to denote a particular value of the quantity $\mathcal{C}$. For example, a yellow circle refers to a droplet diameter calculated under a slip coefficient quantified by 0.05 with an acoustic capillary number given by $\mathcal{C} = 60$, whereas a purple square means a droplet diameter estimated under the no-slip condition with $\mathcal{C} = 40$. Worth to be mention is the presence of inset **A** in Fig. 6(b), which magnifies the region containing our numerical diameter estimations to provide a clearer depiction of our results.

Important considerations can be made from Fig. 6(b), in first place we note d scales linearly respect $(\varepsilon \mathcal{C})^{2/3} f_e$. Such behavior has been reported by Collins *et al.* in the absence of the slippage phenomenon at the wall, then, in view of the results portrayed by Fig. 6(b), we can add that the presence of slippage at the wall does not affect the linear relationship between d and $(\varepsilon \mathcal{C})^{2/3} f_e$. Continuing analyzing Fig. 6(b), we note that—regardless the value of the acoustic capillary number—the diameters developed under the no-slip condition are always bigger than those achieved under the influence of slippage. To validate this assertion, let us situate ourselves at the rightmost side of the regression curve of our numerical data. Then, let us move along such curve from right to left; by doing this, we find in first place a "no-slip region," i.e., a series of square symbols scattered through the interval $1.7 \times 10^{-7} \lesssim (\varepsilon \mathcal{C})^{2/3} f_e \lesssim 2.4 \times 10^{-7}$ s. Such symbols indicate that. Varying $\mathcal{C}$ from 30 to 90 under the no-slip condition. causes the development of droplet diameters in the

proximities of $d = 20 \ \mu$m. Continuing moving ourselves to the left, along the regression curve, we find the "slip region." Such a region comprehends the geometric shapes we have designated for the cases $\beta_0 = 0.05, 0.1, 0.2$ and is developed on the interval $0.6 \times 10^{-7} \lesssim (\varepsilon \mathcal{C})^{2/3} f_e \lesssim 1.7 \times 10^{-7}$, exhibiting smaller droplet diameters than the no-slip cases. In this context, let us note that the cases associated to $\beta_0 = 0.2$ (star symbols) develop the smallest droplet diameters, with d being situated below 10 μm, and therefore are suitable for pulmonary drug delivery applications [22].

At this point let us recall—from our discussion regarding Fig. 3—that increasing the acoustic capillary number beyond the onset of atomization traduces in a major number of liquid threads being formed at the air-liquid interface. Thus, if a major number of aerosol droplets is desired to be ejected from the parent drop, then an increment at $\mathcal{C}$ is desirable. However, the no-slip region depicted in Fig. 6(b) shows that if a reduction of the droplet diameter is required, the quantity $\mathcal{C}$ must be reduced. This situation suggest a conflict between modifying the aerosol characteristic diameter and keeping the rate of atomization of the parent drop above certain limit. In this context, the results provided in Fig. 6(b) shows a valuable application of the slippage phenomenon. To explain such application, let us consider a fixed acoustic capillary number, for example $\mathcal{C} = 50$ [depicted with cyan color in Fig. 6(b)] and vary the slip coefficient. In this sense, we note that a parent drop under $\mathcal{C} = 50$ and $\beta = 0.2$ develops a smaller diameter than a drop with $\mathcal{C} = 50$ and $\beta = 0.0$. As also referred to before, the acoustic capillary number portrays the ratio between the mechanical power (acoustic forcing) exerted on the drop's free surface and the capillary stress. Thus, for a fixed surface tension value, the presence of slippage at the wall allows to reduce the aerosol characteristic diameter without varying $\mathcal{C}$ and therefore the mechanical power exerted at the interface. This behavior can be desirable to control the droplet diameter without affecting the quantity of droplets being ejected from the parent drop.

Next, we address the validation of the numerical model presented on this study. In this context, let us note that, by comparing our numerical estimations for d with the data provided by Collins *et al.* we have found a good correlation between our calculations and the experimental measurements provided at their study. Specifically, the concordance we are referring to lies in the data points plotted in "*Fig. 5(b)*" in Collins' study. Such points, labeled as "*peak 1 data*," consist in several measurements regarding the characteristic diameter of the aerosol being ejected from a water thin film under variable SAW frequencies with $f_e(\text{Hz}) \sim 10^7 – 10^8$ Hz. In this context, the diameter values we show in Fig. 6(b), although developed by considering a fixed SAW frequency on the order 10^7 Hz and the presence of the slippage at the wall, closely follows—qualitatively and quantitatively—the experimental data reported by Collins study. Worth to be mentioned again is that the presence of slippage at the wall does not affect the linear dependence of the droplet diameter against the quantity $(\varepsilon \mathcal{C})^{2/3} f_e$. According to the results plotted in Fig. 6(b), the presence of slip in the formation of aerosol via SAWs simply "translates" the resulting diameter to the left at the curve $d - (\varepsilon \mathcal{C})^{2/3} f_e$. This means that, given a specific value of the acoustic capillary number and a specific excitation frequency, the diameter of the aerosol emerging from the parent drop is smaller than its counterpart developed under the no-slip condition and the magnitude of the slip-coefficient results to be determinant to predict how important is such diameter reduction. Let us note the inclusion of Table II, which explicitly shows the values of our diameter estimations plotted in Fig. 6(b) [Table II(A)] besides the temporal variable, $(\varepsilon \mathcal{C})^{2/3} f^{-1}$ [Table II(B)], at which each diameter estimation was obtained. Such inclusion has been done to facilitate data comparison with respect to Collins *et al.*'s study.

A series of final considerations are made regarding the influence of slippage at the spreading mechanism of the parent drop due to SAW excitation. Specifically, we focus our attention now in measuring the speed of the advancing contact line of our drop model under different values of both, the slip coefficient and the acoustic capillary number. Before discussing our measurements, let us note that the spreading phenomenon exhibited by our drop shapes is caused by the influence of the acoustic radiation, such effect has been modeled during our lubrication-type approach through the term Π_{ac}, i.e., the acoustic pressure. Nevertheless, additional boundary phenomena also take part at the dynamics of the contact line of thin films exposed to SAW excitation, such as Schlichting

TABLE II. (A) Droplet diameter (d) estimations corresponding the data symbols depicted in Fig. 6(b). (B) Temporal variable, $(\varepsilon\mathcal{C})^{2/3}f^{-1}$, at which each droplet diameter has been obtained. Let us note $\mathcal{C}$ is the acoustic capillary number and β_0 is the dimensionless slip coefficient.

	(A) d [μm]			
$\mathcal{C}$ $\diagdown$ β_0	0.0	0.05	0.1	0.2
30	17.17	11.29	9.32	7.11
40	17.92	12.06	9.81	7.30
50	20.33	13.10	10.53	7.88
60	20.80	14.03	11.29	8.17
70	23.05	14.52	11.71	8.45
80	23.48	15.44	12.27	8.79
90	24.65	16.24	12.75	9.32
	(B) $(\varepsilon\mathcal{C})^{2/3}f^{-1}$ [s]			
$\mathcal{C}$ $\diagdown$ β_0	0.0	0.05	0.1	0.2
30	1.717	1.129	0.932	0.711
40	1.792	1.206	0.981	0.730
50	2.033	1.310	1.053	0.788
60	2.080	1.403	1.129	0.817
70	2.305	1.452	1.171	0.845
80	2.348	1.544	1.227	0.879
90	2.465	1.624	1.275	0.932

streaming, acoustic attenuation, and even the influence of intermolecular forces. All of these phenomena are beyond the scope of the lubrication-type approach implemented during our study. Thus, our measurements of the contact line speed should be interpreted as an approximation, developed to qualitatively discuss interesting aspects regarding the influence of slippage at the drop's spreading. In this context, we have developed Fig. 7, which plots the quantity $\bar{V}$ against the dimensionless slip coefficient. Let us recall that our two-dimensional framework places the drop centered at $\bar{x} = 0$ and the contact lines on our numerical simulations spreads symmetrically along both, $\bar{x}$ and $-\bar{x}$ directions (see Figs. 3 and 4), thus, the quantity $\bar{V}$ describes the overall speed at which the contact lines are drawn apart from the $\bar{z}$ axis. Worth to be noted is the fact we have measured the quantity $\bar{V}$ at four dimensionless slip coefficients, $\beta_0 = 0.0, 0.05, 0.1,$ and 0.2. As referred to before, such values correspond, in physical units, to a slip length varying between $\mathcal{O}(10^{-7})$ and $\mathcal{O}(10^{-6})$ m, which is consistent with experimental measurements of the slip length at small-scale systems under hydrophilic conditions [34]. Moreover, the speed of the contact line has been measured under four different values of the acoustic capillary number, i.e., $\mathcal{C} = 10, 40, 60,$ and 90, each one of them is associated with a particular geometric shape, as can been seen in Fig. 7.

Let us, in first instance, analyze the speed values obtained under the case $\beta_0 = 0$. In this context, Fig. 7 shows that varying the acoustic capillary number from 10 toward 90 under the no-slip condition does not traduces in a significant increment of the contact line speed. However, if we fix the slip coefficient at $\beta_0 = 0.2$, then the variation of the acoustic capillary number causes a more significant increase at the speed $\bar{V}$. Thus, as the slip coefficient increases, the advancing contact line speed becomes more dependent respect the variations at the quantity $\mathcal{C}$. Next, let us fix the acoustic capillary number and vary the slip coefficient, in this context, we recall that $\mathcal{C}$ is the ratio between the mechanical stress exerted on the air-liquid interface and the capillary stress. Thus,
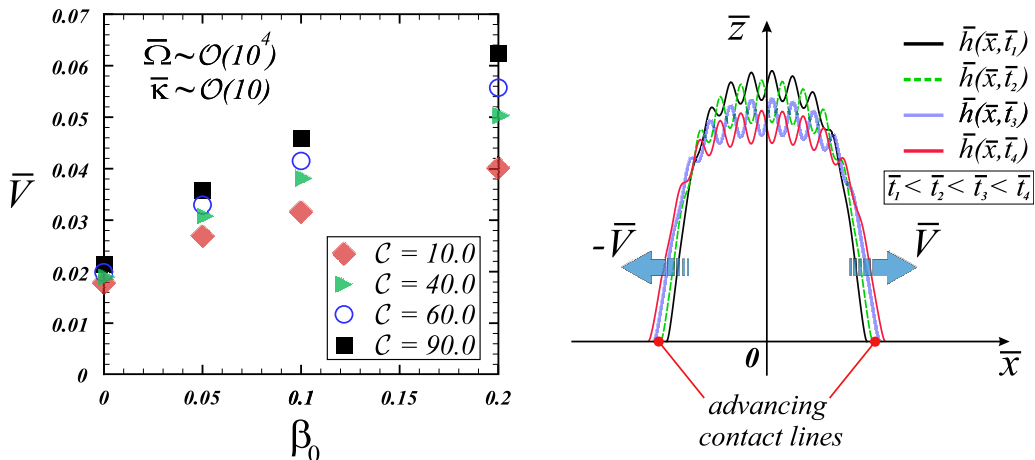
FIG. 7. Numerical measurement of the dimensionless contact line speed, $\bar{V}$, of our drop model under different values of the slip coefficient and the acoustic capillary number. Specifically, $\bar{V}$ is the absolute value of the speed at which the two contact lines of our two-dimensional model symmetrically draw apart from the $\bar{z}$ axis as time progresses. In this context, let us recall we are considering a dimensionless frequency $\bar{\Omega} \sim \mathcal{O}(10^4)$ and a wave number $\bar{\kappa} \sim \mathcal{O}(10)$. Such values, in physical units, correspond to typical excitation parameters with $f_e(\text{Hz}) \sim 10^7$ and $\lambda(\text{m}) \sim 10^{-4}$. Specifically, the contact line speed has been obtained under four different slip coefficients: $\beta_0 = 0.0, 0.05, 0.1$, and 0.2 and under four acoustic capillary numbers.

Fig. 7 also suggests that the presence of slippage phenomenon allows to increase the advancing contact line speed under a constant mechanical power. If we take into account that the characteristic velocity implemented during our lubrication-type approach can be on the order of 10^{-2}–10^{-1} m/s, then the speed values depicted on Fig. 7 correspond to physical values on the order 10^{-1}–1 mm/s. Moreover, we have approximated the parent drop as a thin film with a thickness $H(\text{m}) \sim 10^{-4}$–10^{-5}. Such ranges agree with experimental data reported on specialized literature, which suggest the advancing contact line of thin films under SAW excitation, with thicknesses $H(\text{m}) \sim 10^{-5}$, exhibits a speed on the order 10^{-1} mm/s [59]. In this context, the feasibility of the data depicted in Fig. 7 is demonstrated.

IV. CONCLUSIONS

The present work provides insight about the influence of the Navier slip condition over the interfacial destabilization mechanism preceding the atomization of an air-liquid interface exposed to SAW excitation. In this context, a simplified drop model—based on a lubrication type approach—was developed to depict the spatiotemporal evolution of the free surface of a fluid drop exposed to a high-frequency acoustic standing wave. Such approach allowed us to evaluate, qualitative and quantitatively, the impact of the slip coefficient at the dynamics of the air-liquid interface. The implementation of the Navier slip condition on our drop model was made assuming a scenario at which the substrate placed below the drop has an affinity for water, i.e., hydrophilic conditions have been assumed. Accordingly, during our study we have considered slip coefficients which agree with experimental measurements of slippage under hydrophilic conditions.

Implementation of the Navier slip condition at small-scale systems supposes significant hydrodynamic differences in comparison the classical no-slip condition [32], by considering the results presented on this study, numerical simulation suggests this assertion can also be applied to SAW atomization. Our results show that the presence of slippage phenomenon at the substrate below a drop exposed to excitation via SAWs acts oppositely respect a hydrophobic system, that is characterized for its susceptibility to avoid drop spreading. Moreover, slippage under hydrophilic conditions

affects notoriously the free surface dynamics. In this context, our study suggests that dimensionless slip coefficients with $\mathcal{O}(10^{-2}) \lesssim \beta_0 \lesssim \mathcal{O}(10^{-1})$ considerably enhances the formation of liquid threads at the air-liquid interface, besides drop spreading and the speed of the contact line. We note the dimensionless coefficients used on our numerical simulations can be associated with a slip length in the range $\beta(\mathrm{m}) \sim 10^{-7}$–$10^{-6}$.

The influence of slippage at the free surface dynamics referred to above becomes notorious when evaluating the drop's aspect ratio evolution against time. In this context, our numerical estimation of the function $\varepsilon(\bar{t})$ has delivered important considerations. One of them is the fact slippage allows the development of smaller aspect ratios in comparison the no-slip case. Another important aspect is the development of a quasisteady behavior at the aspect ratio evolution which is strongly linked with the magnitude of the acoustic capillary number. Such behavior has resulted fundamental for the present study at the moment of proposing a power-law relationship between the slip coefficient and the drop's aspect ratio. Such relationship, graphically depicted in Fig. 6(a), has allowed us to be aware that varying the slip coefficient in the range $0.0 < \beta_0 \lesssim 0.1$ causes important variations on the aspect ratio during the quasisteady state. However, varying β_0 beyond 0.1 traduces in slighter variations at ε. If we take into account that previous studies have established that $d = d(\varepsilon)$ [18,49]—where d is the aerosol characteristic diameter—then the interval $0.0 < \beta_0 \lesssim 0.1$ contributes to generate abrupt changes at the droplet diameter whereas varying β_0 beyond 0.1 contribute to a more accurate control of the droplet diameter.

The observations referred to above had led us to estimate the droplet diameter under different slip coefficients and evaluate the utility of slippage phenomenon as a mean to control the aerosol generation during SAW atomization. In the process, the present study have proposed Eq. (41) to predict those droplet diameters developed under slip coefficients above $\beta_0 = 0.01$. The estimations of the droplet diameter obtained through the use of Eq. (41) allow us to assert the slippage allows the development of smaller diameters respect the no-slip case. Perhaps the most relevant behavior encountered during our numerical prediction of the quantity d is the fact the same acoustic capillary number yields, under various slip coefficients, different droplet diameters. This behavior suggest the mechanical power exerted on the parent drop can remain constant at the moment of reducing the droplet diameter below certain limit, through the implementation of a substrate with a certain amount of slippage at its surface.

In the continuous quest for improving the efficiency and design cost of microfluidic devices, proper knowledge of the fundamental mechanism behind their operation is desirable and of sum importance. In the context of SAW atomization, such assertion can be traduced in finding new and efficient means with the capability to modify the drop's resistance toward acoustic deformation and the aerosol properties. In this context, the numerical analysis presented in this study, allow us to postulate slippage as a valuable phenomenon which can influence the free surface dynamics besides the aerosol generation with a direct repercussion on the operation of small-scale atomizers.

APPENDIX: THE SOLUTION METHODOLOGY

The MOL replaces the spatial derivatives with algebraic approximations in the evolution equation to get a system of ordinary differential equations, based on time-dependent values of the film thickness at a discrete set of values of the spatial coordinate $\bar{x}$. After that, an integration algorithm for initial-value ODEs is applied to compute a numerical solution for the evolution equation. The computational domain for Eq. (34) subjected to the boundary condition Eqs. (37) and (38) was $(-L < \bar{x} < L)$, with $L \to \infty$. The value in L was sufficiently large to assure a negligible

deformation at the ends of the drop. In this context, we used $L = 1.5$, so the film is flat near $\bar{x} = \pm L$. At this point, we conveniently rewrite Eq. (34) as

$$\partial_{\bar{t}}\bar{h} = -\partial_{\bar{x}}\bar{Q}, \quad \text{where} \quad \bar{Q} = \left(\tfrac{1}{3}\bar{h}^3 + \beta_0\bar{h}^2\right)\left[\partial_{\bar{x}}^3\bar{h} + 4\bar{\kappa}\,\mathcal{C}\cos(2\bar{\kappa}\bar{x})\cos(2\bar{\Omega}\bar{t})\right], \tag{A1}$$

where Q is the volumetric flux. To discretize the computational domain, we establish a finite-difference grid with N points, divided itself into $N-1$ equal subintervals, each of length $\Delta\bar{x} = 2L/(N-1)$, so that the coordinates of the grid points are $\bar{x}_i = -L + (i-1)\Delta\bar{x}$ with $i = 1, 2, ..., N$. The film thickness at the grid points, denoted by $\bar{h}_i$, is a function of time only and satisfies a system of N first-order ordinary differential equations, defined by

$$\frac{d\bar{h}_i}{d\bar{t}} = -\frac{\bar{Q}_{i+1/2} - \bar{Q}_{i-1/2}}{\Delta\bar{x}}, \tag{A2}$$

where $\bar{Q}_{i\pm1/2}$ are the approximate values of $\bar{Q}$ at the points half-way between grid points $\bar{x}_{i\pm1/2} = \bar{x}_i \pm \Delta\bar{x}/2$. In this context, two finite difference approximations for the evolution equation at each side of the gridpoint x_i are defined:

$$\bar{Q}_{i+1/2} = \frac{1}{6(\Delta\bar{x})^3}\left[\left(\bar{h}_i^3 + \bar{h}_{i+1}^3\right) + 3\beta_0\left(\bar{h}_i^2 + \bar{h}_{i+1}^2\right)\right]$$
$$\times\,\left[(\bar{h}_{i+2} - 3\bar{h}_{i+1} + 3\bar{h}_i - \bar{h}_{i-1}) + 4\bar{\kappa}(\Delta\bar{x})^3\,\mathcal{C}\cos(2\bar{\kappa}\bar{x}_{i+\frac{1}{2}})\cos(2\bar{\Omega}\bar{t})\right] \tag{A3}$$

and

$$\bar{Q}_{i-1/2} = \frac{1}{6(\Delta\bar{x})^3}\left[\left(\bar{h}_i^3 + \bar{h}_{i-1}^3\right) + 3\beta_0\left(\bar{h}_i^2 + \bar{h}_{i-1}^2\right)\right]$$
$$\times\,\left[(\bar{h}_{i+1} - 3\bar{h}_i + 3\bar{h}_{i-1} - \bar{h}_{i-2}) + 4\bar{\kappa}(\Delta\bar{x})^3\,\mathcal{C}\cos(2\bar{\kappa}\bar{x}_{i-\frac{1}{2}})\cos(2\bar{\Omega}\bar{t})\right]. \tag{A4}$$

In Eqs. (A3) and (A4), a standard second-order centered finite difference approximation of the third derivative at the point $\bar{x}_{i+1/2}$ has been used. Note that, for the inner values of i (i.e., for i varying from 3 to $N-2$), Eqs. (A3) and (A4) can be directly implemented, however, at the endpoints of the computational domain ($i = 1, 2, N-1$, and N), one needs points that are located outside the domain (the so-called *fictitious* or *ghost points*) to evaluate the spatial derivatives when using centered finite difference approximations. The system of Eqs. (A2) with the initial condition Eq. (36) is solved using a standard differential equation solver. It is worth to reconsider the initial condition Eq. (36) and address its suitability to depict a drop in an undeformed state. In this sense, our numerical simulation based on this initial profile will "adjust" the initial geometry regarding the drop's interface, before proceeding with the actual simulation of the capillary waves formed during SAW excitation.

A key aspect to take into account during the numerical solution of Eq. (A2) is the presence of different time scales embedded in this equation system. There exists a time scale for the acoustic stress exerted on the air-liquid interface, associated with the inverse of the harmonic excitation frequency, Ω. However, the viscous-capillary response of the fluid possesses a different time scale, defined by $L/U \sim \mu L/\epsilon^2\sigma$, that has been considered in the definition of the dimensionless time, $\bar{t}$. Considering the above, Eq. (A2) constitutes a system of equations that is said to be *stiff* [55,60]. In this context, we use the standard MATLAB *solver ode15s* for stiff systems of ordinary differential equations to obtain the Spatiotemporal liquid-air interface evolution of a drop under SAW excitation with slippage at the solid wall.

Note that the evolution Eq. (34) and its approximation Eq. (A2) derive from the principle of conservation of mass of the liquid, thus, in our two-dimensional framework, the numerical solution for $\bar{h}(\bar{x}, \bar{t})$ must attend this principle through the conservation of the area under the curve, defined by

$$\int_{-L}^{L} \bar{h}\, d\bar{x}. \tag{A5}$$

To demonstrate that the area under the curve of $\bar{h}$ is preserved by our numerical method, let us approximate the integral Eq. (A5) by using the trapezoid rule

$$I = \sum_{i=1}^{N-1} \frac{1}{2} \Delta \bar{x} (\bar{h}_i + \bar{h}_{i+1}), \tag{A6}$$

where the quantity I was introduced to denote the numerical approximation of the area under the curve. We differentiate I respect to $\bar{t}$, and combining with Eq. (A2), it yields

$$\frac{dI}{d\bar{t}} = \frac{1}{2}(\bar{Q}_{1/2} + \bar{Q}_{3/2} - \bar{Q}_{N-1/2} - \bar{Q}_{N+1/2}). \tag{A7}$$

The four terms at the right-hand side of Eq. (A7) are equal to zero since $i = 1/2, 3/2, N - 1/2, N + 1/2$ correspond to a region ($\bar{x} \approx \pm L$), where the film is flat and the symmetry condition Eqs. (37) and (38) have been imposed. Thus, the value of I is expected to be conserved during our numerical simulations.

Through a *consistency analysis* [60], implemented in Eqs. (A3) and (A4), it is possible to approximate $\partial \bar{Q} / \partial \bar{x}$ as a second-order accurate in space. The grid size used for the numerical solutions was defined by running the code for several different values of N using a subsequent evaluation of the norm of the error for the numerical solution of the discretized system at a fixed time, given by the following expression:

$$E = \left[\Delta \bar{x} \sum_{i=1}^{N} (\bar{h}_i^N - \bar{h}_i^f)^2 \right]^{1/2}. \tag{A8}$$

The fixed time was considered at $\bar{t} = 0.5$, a sufficiently large time for the interfacial vibration mechanism to be fully developed, in view that there exists an initial transient during the numerical solution startup (developed at $0 < \bar{t} < 0.18$) before the simulation of the acoustic interfacial deformations truly commences (see Sec. III for more details). In Eq. (A8), $\bar{h}_i^N$ and $\bar{h}_i^f$ are the numerical solutions obtained on a grid of N points and the finest grid used in our simulations, respectively. The difference between $\bar{h}_i^f$ and the (unknown) exact solution is assumed to be negligible when estimating the error norm. Thus, by implementing Eq. (A8), a desirable spatial error norm of the order $E \sim \mathcal{O}(10^{-6})$ has been found to correspond a finite-difference grid of $N = 300$ points, laid in the previously closed domain $-1.5 \leqslant \bar{x} \leqslant 1.5$, yielding a right balance between computational effort and precision. The tolerances for the time-stepping routine implemented in the solver ode15s from MATLAB are chosen small enough, so that the error associated with the time-discretization process is negligible in comparison with the contribution to the error because of the approximation of spatial derivatives; in this context, a relative tolerance and an absolute tolerance of $\mathcal{O}(10^{-4})$ and $\mathcal{O}(10^{-20})$ were chosen, respectively.

---

[1] D. Mark, S. Haeberle, G. Roth, F. von Stetten, and Roland Zengerle, Microfluidic lab-on-a-chip platforms: Requirements, characteristics, and applications, Chem. Soc. Rev. **39**, 1153 (2010).

[2] H. A. Stone, A. D. Stroock, and A. Ajdari, Engineering flows in small devices: Microfluidics toward a lab-on-a-chip, Annu. Rev. Fluid Mech. **36**, 381 (2004).

[3] F. Alnaimat, S. Dagher, B. Mathew, A. Hilal-Alnqbi, and S. Khashan, Microfluidics based magnetophoresis: A review, Chem. Rec. **18**, 1 (2018).

[4] R. Pethig, Review article-dielectrophoresis: Status of the theory, technology, and applications, Biomicrofluidics **4**, 022811 (2010).

[5] H. Bruus, J. Duall, J. Hawkes, M. Hill, T. Laurell, J. Nilsson, S. Radel, S. Sadhal, and M. Wiklund, Forthcoming laboratory on a chip tutorial series on acoustofluidics: Acoustofluidics-exploiting ultrasonic

standing wave forces and acoustic streaming in microfluidic systems for cell and particle manipulation, Lab Chip **11**, 3579 (2011).

[6] J. Friend and L. Y. Yeo, Microscale acoustofluidics: Microfluidics driven via acoustics and ultrasonics, Rev. Mod. Phys. **83**, 647 (2011).

[7] K. D. Frampton, S. E. Martin, and K. Minor, The scaling of acoustic streaming for application in microfluidic devices, Appl. Acoust. **64**, 681 (2003).

[8] A. Nilsson, F. Petersson, H. Jönsson, and T. Laurell, Acoustic control of suspended particles in micro fluidic chips, Lab Chip **4**, 131 (2004).

[9] R. M. White and F. W. Voltmer, Direct piezoelectric coupling to surface elastic waves, Appl. Phys. Lett. **7**, 314 (1965).

[10] R. J. Lang, Ultrasonic atomization of liquids, J. Acoust. Soc. Am. **34**, 6 (1962).

[11] F. Barreras, H. Amaveda, and A. Lozano, Transient high-frequency ultrasonic water atomization, Exp. Fluids **33**, 405 (2002).

[12] G. Biskos, V. Vons, C. U. Yurteri, and A. Schmidt-Ott, Generation and sizing of particles for aerosol-based nanotechnology, KONA Powder Particle J. **26**, 13 (2008).

[13] C. B. Felder, M. J. Blanco-Prieto, J. Heizmann, H. P. Merkle, and B. Gander, Ultrasonic atomization and subsequent polymer desolvation for peptide and protein microencapsulation into biodegradable polyesters, J. Microencapsul. **20**, 553 (2003).

[14] G. Forde, J. Friend, and T. Williamson, Straightforward Biodegradable Nanoparticle Generation Through Megahertz-Order Ultrasonic Atomization, Appl. Phys. Lett. **89**, 064105 (2006).

[15] M. Alvarez, J. Friend, and L. Y. Yeo, Rapid generation of protein aerosols and nanoparticles via surface acoustic wave atomization, Nanotechnology **19**, 455103 (2008).

[16] K. M. Ang, L. Y. Yeo, J. R. Friend, Y. M. Hung, and M. K. Tan, Nozzleless spray cooling using surface acoustic waves, J. Aerosol Sci. **79**, 48 (2015).

[17] M. Kurosawa, T. Watanabe, A. Futami, and T. Higuchi, Surface acoustic wave atomizer, Sensors Actuators **50**, 69 (1995).

[18] A. Qi, L. Y. Yeo, and J. R. Friend, Interfacial destabilization and atomization driven by surface acoustic waves, Phys. Fluids **20**, 074103 (2008).

[19] A. Qi, J. R. Friend, L. Y. Yeo, D. A. V. Morton, M. P. McIntosh, and L. Spiccia, Miniature inhalation therapy platform using surface acoustic wave microfluidic atomization, Lab Chip **9**, 2184 (2009).

[20] A. Qi, L. Yeo, J. Friend, and J. Ho, The extraction of liquid, protein molecules and yeast cells from paper through surface acoustic wave atomization, Lab Chip **10**, 470 (2010).

[21] A. Rajapaksa, A. Qi, L. Y. Yeo, R. Coppel, and J. R. Friend, Enabling practical surface acoustic wave nebulizer drug delivery via amplitude modulation, Lab Chip **14**, 1858 (2014).

[22] A. E. Rajapaksa, J. J. Ho, A. Qi, R. Bischof, T. H. Nguyen, M. Tate, D. Piedrafita, M. P. McIntosh, L.Y. Yeo, E. Meeusen, R. L. Coppel, and J. R. Friend, Effective pulmonary delivery of an aerosolized plasmid dna vaccine via surface acoustic wave nebulization, Respir. Res. **15**, 60 (2015).

[23] X. Ding, P. Li, S. S. Lin, Z. S. Stratton, N. Nama, F. Guo, D. Slotcavage, X. Mao, J. Shi, F. Costanzo, and T. J. Huang, Surface acoustic wave microfluidics, Lab Chip **13**, 3626 (2013).

[24] A. Wixforth, C. Strobl, Ch. Gauer, A. Toegl, J. Scriba, and Z. v. Guttenberg, Acoustic manipulation of small droplets, Anal. Bioanal. Chem. **379**, 982 (2004).

[25] L. G. Leal, *Advanced Transport Phenomena* (Cambridge University Press, Cambridge, UK, 2007).

[26] S. R. Heron, R. Wilson, S. A. Shaffer, D. R. Goodlet, and J. M. Cooper, Surface acoustic wave nebulization of peptides as a microfluidic interface for mass spectrometry, Anal. Chem. **82**, 3985 (2010).

[27] A. W. Martinez, S. T. Phillips, M. J. Butte, and G. M. Whitesides, Patterned paper as a platform for inexpensive, low-volume, portable bioassays, Angew. Chem. Int. Ed. **46**, 1318 (2007).

[28] J. Blamey, L. Y. Yeo, and J. R. Friend, Microscale capillary wave turbulence excited by high frequency vibration, Langmuir **29**, 3835 (2013).

[29] M. Schindler, P. Talkner, and P. Hanggi, Computing stationary free-surface shapes in microfluidics, Phys. Fluids **18**, 103303 (2006).

[30] D. Koster, Numerical simulation of acoustic streaming on surface acoustic wave-driven biochips, SIAM J. Sci. Comput. **29**, 2352 (2007).

[31] M. K. Tan, J. R. Friend, O. K. Matar, and L. Y. Yeo, Capillary wave motion excited by high frequency surface acoustic waves, Phys. Fluids **22**, 112112 (2010).

[32] E. Lauga, M. Brenner, and H. Stone, *Microfluidics: The No-slip Boundary Condition* (Springer, Berlin, 2007).

[33] K. Watanabe, Yanuar, and H. Udagawa, Drag reduction of newtonian fluid in a circular pipe with a highly water-repellent wall, J. Fluid Mech. **381**, 225 (1999).

[34] C. Tropea, A. L. Yarin, and J. F. Foss (Eds.), *Handbook of Experimental Fluid Mechanics* (Springer-Verlag, Berlin, 2007).

[35] E. Bonaccurso, H. J. Butt, and V. S. J. Craig, Surface Roughness and Hydrodynamic Boundary Slip of a Newtonian Fluid in a Completely Wetting System, Phys. Rev. Lett. **90**, 144501 (2003).

[36] E. Bonaccurso, M. Kappl, and H. J. Butt, Hydrodynamic Force Measurements: Boundary Slip of Water on Hydrophilic Surfaces and Electrokinetic Effects, Phys. Rev. Lett. **88**, 076103 (2002).

[37] H. Hervet and L. Léger, Flow with slip at the wall: From simple to complex fluids, C. R. Physique **4**, 241 (2003).

[38] R. Pit, H. Hervet, and L. Léger, Friction and slip of a simple liquid at a solid surface, Trib. Lett. **7**, 147 (1999).

[39] J. Baudry, E. Charlaix, A. Tonk, and D. Mazuyer, Experimental evidence for a large slip effect at a nonwetting fluid-solid interface, Langmuir **17**, 5232 (2001).

[40] C. Cheikh and G. Koper, Stick-Slip Transition at the Nanometer Scale, Phys. Rev. Lett. **91**, 156102 (2003).

[41] C. H. Choi, K. Johan, A. Westin, and K. S. Breuer, Apparent slip flows in hydrophillic and hydrophobic microchannels, Phys. Fluids **15**, 2897 (2003).

[42] C. Cottin-Bizonne, S. Jurine, J. Baudry, J. Crassous, F. Restagno, and É. Charlaix, Nanorheology: An investigation of the boundary condition at hydrophobic and hydrophilic interfaces, Eur. Phys. J. E **9**, 47 (2002).

[43] V. S. J. Craig, C. Neto, and D. R. M. Williams, Shear-Dependent Boundary Slip in an Aqueous Newtonian Liquid, Phys. Rev. Lett. **87**, 054504 (2001).

[44] P. Joseph and P. Tabeling, Direct measurement of the apparent slip length, Phys. Rev. E **71**, 035303(R) (2005).

[45] D. Lumma, A. Best, A. Gansen, F. Feuillebois, J. O. Rädler, and O. I. Vinogradova, Flow profile near a wall measured by double-focus fluorescence cross-correlation, Phys. Rev. E **67**, 056313 (2003).

[46] Y. Zhu and S. Granick, Limits of the Hydrodynamic No-Slip Boundary Condition, Phys. Rev. Lett. **88**, 106102 (2002).

[47] M. Darmawan and D. Byun, Focused surface acoustic wave induced jet formation on superhydrophobic surfaces, Microfluid Nanofluid **18**, 1107 (2015).

[48] M. K. Tan, J. R. Friend, and L. Y. Yeo, Interfacial Jetting Phenomena Induced by Focused Surface Vibrations, Phys. Rev. Lett. **103**, 024501 (2009).

[49] D. J. Collins, O. Manor, A. Winkler, H. Schmidt, J. R. Friend, and L. Y. Yeo, Atomization off thin water films generated by high-frequency substrate wave vibrations, Phys. Rev. E **86**, 056312 (2012).

[50] S. Kalliadasis and H.-C. Chang, Dynamics of liquid spreading on solid surfaces, Ind. Eng. Chem. Res **35**, 2860 (1996).

[51] L. Y. Yeo and H.-C. Chang, Electrowetting films on parallel line electrodes, Phys. Rev. E **73**, 011605 (2006).

[52] L. Rayleigh, On waves propagated along the plane surface of an elastic solid, Proc. London Math. Soc. **4**, s1 (1885).

[53] Lord Rayleigh, On the momentum and pressure of gaseous vibrations, and on the connexion with the virial theorem, Philos. Mag. **10**, 364 (1905).

[54] W. L. M. Nyborg, *Acoustic Streaming, Volume 2, Part B* (Academic Press, San Diego, CA, 1965).

[55] W. E. Schiesser and G. W. Griffiths, *A Compendium of Partial Differential Equation Models: Method of Lines Analysis with Matlab* (Cambridge University Press, Cambridge, UK, 2009).

[56] V. S. Ajaev, *Interfacial Fluid Mechanics: A Mathematical Modeling Approach* (Springer, Berlin, 2012).

[57] M. Alvarez, L. Y. Yeo, J. R. Friend, and M. Jamriska, Rapid production of protein-loaded biodegradable microparticles using surface acoustic waves, Biomicrofluidics **3**, 014102 (2009).

[58] H. Li, J. R. Friend, and L. Y. Yeo, Microfluidic Colloidal Island Formation and Erasure Induced by Surface Acoustic Wave Radiation, Phys. Rev. Lett. **101**, 084502 (2008).

[59] A. R. Rezk, O. Manor, J. R. Friend, and L. Y. Yeo, Unique fingering instabilities and soliton-like wave propagation in thin acoustowetting films, Nat, Commun. **3**, 1167 (2012).

[60] J. D. Hoffman, *Numerical Methods for Engineers and Scientists* (Marcel Dekker, New York, NY, 2001).